Model Bias Reduction and the Limits of Oceanic Decadal Predictability: Importance of the Deep Ocean

FLORIAN SÉVELLEC

Ocean and Earth Science, National Oceanographic Centre Southampton, University of Southampton, Southampton, United Kingdom

ALEXEY V. FEDOROV

Department of Geology and Geophysics, Yale University, New Haven, Connecticut

(Manuscript received 5 April 2012, in final form 14 November 2012)

ABSTRACT

Ocean general circulation models (GCMs), as part of comprehensive climate models, are extensively used for experimental decadal climate prediction. Understanding the limits of decadal ocean predictability is critical for making progress in these efforts. However, when forced with observed fields at the surface, ocean models develop biases in temperature and salinity. Here, the authors ask two complementary questions related to both decadal prediction and model bias: 1) Can the bias be temporarily reduced and the prediction improved by perturbing the initial conditions? 2) How fast will such initial perturbations grow? To answer these questions, the authors use a realistic ocean GCM and compute temperature and salinity perturbations that reduce the model bias most efficiently during a given time interval. The authors find that to reduce this bias, especially pronounced in the upper ocean above 1000 m, initial perturbations should be imposed in the deep ocean (specifically, in the Southern Ocean). Over 14 yr, a 0.1-K perturbation in the deep ocean can induce a temperature anomaly of several kelvins in the upper ocean, partially reducing the bias. A corollary of these results is that small initialization errors in the deep ocean can produce large errors in the upper-ocean temperature on decadal time scales, which can be interpreted as a decadal predictability barrier associated with ocean dynamics. To study the mechanisms of the perturbation growth, the authors formulate an idealized model describing temperature anomalies in the Southern Ocean. The results indicate that the strong mean meridional temperature gradient in this region enhances the sensitivity of the upper ocean to deep-ocean perturbations through nonnormal dynamics generating pronounced stationary-wave patterns.

1. Introduction

Experimental decadal climate prediction [or ''near term'' in the language of the Intergovernmental Panel on Climate Change (IPCC)] is an active area of research with the issues of decadal predictability being now thoroughly explored (e.g., Meehl et al. 2009). Ensemble experiments generating decadal climate hindcasts have become an important component of the phase 5 of the Coupled Model Intercomparison Project (CMIP5) protocol and a part of the upcoming IPCC climate assessment [Fifth Assessment Report (AR5); Taylor et al. 2012]. The present study looks at the problem of decadal predictability in the context of the transient growth of temperature and salinity anomalies in the ocean. Specifically, we will demonstrate that anomalies in the deep ocean are critical for changes in the upper ocean and hence for climate prediction on decadal time scales.

Historically, different authors approach the problem of decadal predictability from several directions. Many studies focus on the dominant modes of decadal climate variability. Such modes, reflecting a deterministic part of the system, provide a potential source of predictability. For example, using a coupled ocean–atmosphere general circulation model (GCM), Latif and Barnett (1996) showed potential predictability on decadal time scales due to the existence of a natural mode of variability in the North Pacific. Another study (Griffies and Bryan 1997) demonstrated that the predictability of climate in

Corresponding author address: Florian Sévellec, Ocean and Earth Sciences, University of Southampton, Waterfront campus, European Way, Southampton SO14 3ZH, United Kingdom.
E-mail: florian.sevellec@noc.soton.ac.uk

DOI: 10.1175/JCLI-D-12-00199.1

the North Atlantic could reach 10–20 yr in a Geophysical Fluid Dynamics Laboratory (GFDL) coupled climate model. The latter authors described three physical mechanisms affecting predictability, including the integration of the synoptic noise in the regions of deep-water formation [following the original idea of Hasselmann (1976)], the dynamics of the Atlantic meridional overturning circulation (AMOC) that controls dominant time scales of decadal climate variability, and the effect of periodic freshwater pulses from the polar regions. More recently, Sévellec and Fedorov (2013a) rigorously confirmed the existence of a damped oscillatory interdecadal mode (an eigenmode) in the North Atlantic controlled solely by ocean dynamics.

With more resources available for computations, direct approaches using ensemble experiments are now broadly used to study decadal predictability. In particular, these approaches can test the sensitivity of predictions to the initial conditions in climate models by looking at the ensemble spread. This follows the ideas of Lorenz (1963) on the chaotic nature of the atmosphere dynamics and error growth after initialization (cf. Strogatz 1994). In this context, Grötzner et al. (1999) used ensemble forecast experiments with a global coupled ocean–atmosphere general circulation model and showed that in their model decadal predictability existed for the processes related to the thermohaline circulation (THC; a component of the AMOC that depends on large-scale thermal and haline gradients), whereas predictability of surface temperatures was marginal in their study (on the order of a year). Ensemble experiments with a coupled GCM by Collins and Sinha (2003) also suggested that the strength of the thermohaline circulation could be predictable over 1–2 decades. At the same time, Pohlmann et al. (2004) did observe predictability of sea surface temperatures (SSTs) in the North Atlantic even on multidecadal time scales but no predictability of surface air temperatures over land (except in some maritime regions of Europe).

In a review paper, Latif et al. (2006) argue that thus far, on decadal time scales, internal climate variability has dominated anthropogenic climate change and that a large fraction of this decadal variability is associated with AMOC variations, whose predictability could possibly extend to two decades in the North Atlantic. Nevertheless, the limits of decadal climate predictability have not been firmly established. In fact, even the AMOC predictability varies from one model to the next and can vary between different time intervals even within a single model (N. S. Keenlyside 2011, personal communication).

A number of studies looked at ways to increase the accuracy of decadal climate predictions. Assimilating the observational data to initialize the ocean model state (Smith et al. 2007) showed an improvement in climate prediction for the next few decades. A crucial step is to synchronize the internal variability of the model with that in the observations. For example, Keenlyside et al. (2008) used an SST relaxation toward observations in coupled models during the initialization procedure, which would allow increasing the model prediction skill.

Following the work on error growth by Lorenz (1965), Palmer (1999) suggested using singular value decomposition (SVD) to identify the most sensitive regions of the ocean (in terms of error growth) and enhance data collection in those regions. The error growth is typically related to the nonnormal properties of dynamical systems (e.g., Farrell and Ioannou 1996a). The use of SVD was also discussed by Tziperman and Ioannou (2002) and Zanna and Tziperman (2005) in the context of the THC.

Using a linear inverse modeling approach (LIM) based on comprehensive coupled GCM, Tziperman et al. (2008) and Hawkins and Sutton (2009a) identified the regions of the North Atlantic especially important for error growth in their models. At the same time, Zanna et al. (2011) stressed the role of the deep ocean in an ocean-only model using an idealized configuration of the North Atlantic (a rectangle, symmetric with respect to the equator basin with a flat bottom).

Considering THC variations, Sévellec et al. (2007) proposed a different methodology, based on optimization approach, which allows for the identification of the regions of the ocean that are most sensitive to initial perturbations. The formulation of this method involves a sensitivity analysis using an adjoint model (e.g., Marotzke et al. 1988) but, unlike SVD, allows more general optimal initial perturbations. Applying this method to a realistic ocean GCM, Sévellec and Fedorov (2013b, manuscript submitted to *Prog. Oceanogr.*) showed that the region of the North Atlantic centered south of the Denmark Strait, east of Greenland, is especially important for exciting decadal variations of the AMOC, which emphasizes the need for an enhanced measurement program in that region.

In a related context, Wunsch (2010) pointed to the long time scales relevant for climate research extending beyond the typical human work and even lifespan. For example, sensitivity analyses of the AMOC reveal the importance of interannual (Tziperman et al. 2008; Zanna and Tziperman 2008; Heimbach et al. 2011), interdecadal (Sévellec et al. 2008; Czeschel et al. 2010), and longer time scales (Sévellec and Fedorov 2013b, manuscript submitted to *Prog. Oceanogr.*). Thus, for a substantial breakthrough in scientific knowledge, multigenerational efforts are necessary.

The previous IPCC report (AR4) summarized climate projections for the twenty-first century, obtained by

integrating coupled GCMs over the period 1950–2100 with different scenarios of future CO_2 emissions (Solomon et al. 2007). Uncertainties in these projections are related to three major factors: deviations between different models, internal variability in each model, and different emission scenarios. Hawkins and Sutton (2009b) demonstrated that, by the end of the twenty-first century, uncertainties related to different emission scenarios dominate. However, for projections on shorter time scales and for decadal climate prediction in particular, the causes of uncertainty are notably different. Within a particular climate GCM (Stone 2004) these causes include the model internal variability, the model bias related to deficiencies in parameterizations of subgrid processes, and errors in model initialization. Here, we will focus on the latter two causes.

The goals of the present study are twofold. First, we will describe a method for reducing bias in the model ocean by modifying the initial conditions for numerical experiments (the bias is defined as the difference between the oceanic observational data and the model output at a given time interval in the future). This could potentially increase the accuracy of decadal forecasting.

Second, we will describe a fundamental physical mechanism that explains how small initial perturbations in the deep ocean are able to induce large changes in the upper-ocean temperature on decadal time scales. This is the mechanism that makes it possible to reduce the model bias efficiently (although temporarily). On the other hand, the exact same mechanism implies that small initial errors in the deep ocean can lead to large errors in the upper ocean within a decade or so of numerical simulations.

When describing this mechanism, we will identify the regions of the deep ocean especially sensitive to error growth (specifically, certain regions of the Southern Ocean). In the Southern Ocean, deep-ocean anomalies stimulate a large-scale stationary wave pattern in the upper ocean corresponding to steady meanders of the Antarctic Circumpolar Current. Such stationary eddies contribute to meridional eddy heat flux (complementing transient eddies; e.g., Olbers et al. 2004) and are important for maintaining the density structure of the Southern Ocean in a steady state (Gnanadesikan and Hallberg 2000; Hallberg and Gnanadesikan 2001).

To achieve the objectives of this study, we will use a generalized stability analysis. Variations of this method have been applied previously to study different problems of ocean dynamics, including mesoscale eddies (Rivière et al. 2001), El Niño–Southern Oscillation (Moore et al. 2003; Sévellec and Fedorov 2010), SST variations in the tropical Atlantic (Zanna et al. 2010), and stability of western boundary currents (Farrell and Moore 1992). This method is particularly useful for predictability studies. For example, it was used to detect the spring predictability barrier in the context of ENSO (Sévellec and Fedorov 2010). Also, this method can be applied for the data targeting and can help reduce errors in the forecasts of the tracks of tropical cyclone (Zhou and Mu 2011; Qin and Mu 2011).

The structure of this paper is as follows: In section 2 we will describe the ocean model and its climatological mean state. In section 3, we will explain the method we use to reduce the model bias in the ocean. We will also discuss major implications of the method and the limitations of linear and weakly nonlinear approaches. In section 4, we formulate an idealized two-level model to elucidate the physical mechanisms relevant to the sensitivity analysis. Section 5 concludes this study.

2. Models and experiments

a. The ocean models and configuration

In this study we employ a broadly used ocean GCM, the Océan Parallélisé (OPA) 8.2 (Madec et al. 1998) in its 2° global configuration (ORCA2; Madec and Imbard 1996). The model has 31 levels in the vertical. The thickness of the model layers varies from 10 m at the surface to 500 m at depth. The rigid-lid approximation is used. The model is integrated using an Arakawa C grid and the z coordinates.

Although some of the models in the next IPCC report (AR5) use a 0.25° resolution for the ocean, in our study we use a configuration with a lower resolution of 2°. The main reason for using the relatively coarse resolution in this study is to avoid baroclinic instability that develops at smaller scales in eddy-permitting or eddy-resolving models. In a linear framework, as introduced in the next sections, such instability could not saturate and would contaminate our calculations. Note that the Institut Pierre-Simon Laplace Coupled Model, version 5 (IPSL CM5), which has OPA as the oceanic component, uses the same 2° resolution (Marti et al. 2010).

The present model configuration utilizes the following parameterizations: convection is parameterized by an increase in the vertical diffusion when the ocean vertical stratification is unstable; double diffusion is taken into account by two different terms for mixing temperature and salinity; eddy-induced velocities are described by the Gent and McWilliams (1990) approximation; the coefficients of eddy viscosity follow the turbulent closure scheme of Blanke and Delecluse (1993) and are functions of longitude, latitude, and depth; and tracer diffusivities for temperature and salinity vary in longitude and latitude (Redi 1982).

The linear and adjoint models are provided by the OPA Tangent Adjoint Model (OPATAM) code (Weaver et al. 2003). The tangent linear model is a linearization of the OPA's primitive equations of motions with respect to the seasonally varying basic state of the ocean. The model and the computational approach generally follow the previous studies of the same authors (Sévellec and Fedorov 2010, 2013a, 2013b, manuscript submitted to *Prog. Oceanogr.*).

In the present study, we use either the flux boundary conditions (surface heat and freshwater fluxes are specified) or mixed boundary conditions (surface heat fluxes are given by a restoring term with the restoring coefficient set to 40 W m^{-2} K^{-1}, while freshwater fluxes are specified). The model climatological surface fluxes are computed by running the full nonlinear GCM forced with a combination of the observed climatological fluxes and weak restoring terms (restoring to the observed climatological seasonal cycle). This approach produces a realistic seasonal cycle for the linear and adjoint models while reducing the damping and allowing SST anomalies to develop more easily for the flux boundary condition (Huck and Vallis 2001; Arzel et al. 2006; Sévellec et al. 2009); for details, see below.

Several additional approximations have been introduced for the tangent-linear and adjoint models: viscosity coefficients in the momentum equations, tracer diffusivities, and the eddy-induced advection are calculated only for the basic ocean state. Further variations in those coefficients are neglected.

b. The model seasonal cycle

The seasonally varying basic state of the ocean, also referred to as the annual model "trajectory," is obtained by the direct integration of the OPA subject to climatological surface boundary forcing (varying with the annual cycle). In particular, we used the European Centre for Medium-Range Weather Forecasts (ECMWF) heat fluxes averaged in the interval from 1979 to 1993, the European Remote-Sensing Satellite (ERS) wind stress blended with the TAO data between 1993 and 1996, and an estimate of the climatological river runoff. In addition, we applied a surface temperature restoring to the Reynolds climatological values averaged from 1982 to 1989, together with a surface salinity restoring to the Levitus (1989) climatology (we emphasize that the restoring term can be switched off in the experiments with the tangent linear and adjoint models). A mass restoring term to the Levitus climatological values of temperature and salinity was applied in the Red and Mediterranean Seas. Starting with the Levitus climatology as the initial conditions, the model produces a quasi-stationary annual cycle of the ocean basic state after 200 yr of integration.

The Atlantic meridional overturning circulation in the full ocean GCM (Fig. 1) is characterized by a northward mass transport above the thermocline, a southward return flow between 1500 and 3000 m, and a recirculation cell below 3000 m associated with the Antarctic Bottom Water (AABW). The maximum volume transport of the AMOC is around 14 Sv (1 Sv $\equiv 10^6$ m^3 s^{-1}), which is slightly below the mean but still within the error bars of the observations (e.g., 18 ± 5 Sv; Talley et al. 2003). The AMOC poleward heat transport reaches 0.8 PW at 25°N, whereas estimates from inverse calculations and hydrographic sections give 1.3 PW at 24°N (Ganachaud and Wunsch 2000).

As expected, the SST field develops a strong meridional gradient in the northern Atlantic, especially across the North Atlantic Current (NAC); there is a salinity maximum at about 20°N (Fig. 1). The plot of barotropic streamfunction shows an intense subtropical gyre and a weaker subpolar gyre centered at about 60°N. The two gyres are separated by the Gulf Stream and the NAC. In the next sections, we will identify the regions with the strongest discrepancy between the observed ocean data (Levitus climatology) and the model output (the model basic state): that is, the model mean bias.

3. Sensitivity of the data–model discrepancy to initial perturbations

The prognostic equations that describe the perturbed trajectory of the model can be rewritten as a general nonautonomous dynamical system,

$$d_t|\mathbf{V}\rangle = \mathcal{N}(|\mathbf{V}\rangle, t), \tag{1}$$

where $\mathcal{N}$ is a time-dependent nonlinear operator and $|\mathbf{V}\rangle$ is the state vector consisting of all prognostic variables. We also define $\langle\mathbf{V}|$ through the Euclidian scalar product $\langle\mathbf{V} \mid \mathbf{V}\rangle$. The state vector can be decomposed as $|\mathbf{V}\rangle = |\overline{\mathbf{V}}\rangle + |\mathbf{v}\rangle$, where $|\overline{\mathbf{V}}\rangle$ is the nonlinear annual trajectory of the model and $|\mathbf{v}\rangle$ is a perturbation (the main notations used in this study are summarized in Table 1).

The time evolution of the perturbation is described by

$$d_t|\mathbf{v}\rangle = \mathbf{A}(t)|\mathbf{v}\rangle, \quad \mathbf{A}(t) = \left.\frac{\partial\mathcal{N}}{\partial|\mathbf{V}\rangle}\right|_{|\overline{\mathbf{V}}\rangle}, \tag{2}$$

where $\mathbf{A}(t)$ is the Jacobian matrix evaluated for a particular value of $|\overline{\mathbf{V}}\rangle$. Integrating this equation from the initial time t_i to the final time t_f, we obtain the perturbation $|\mathbf{v}\rangle$ as a function of time (Farrell and Ioannou 1996b) as

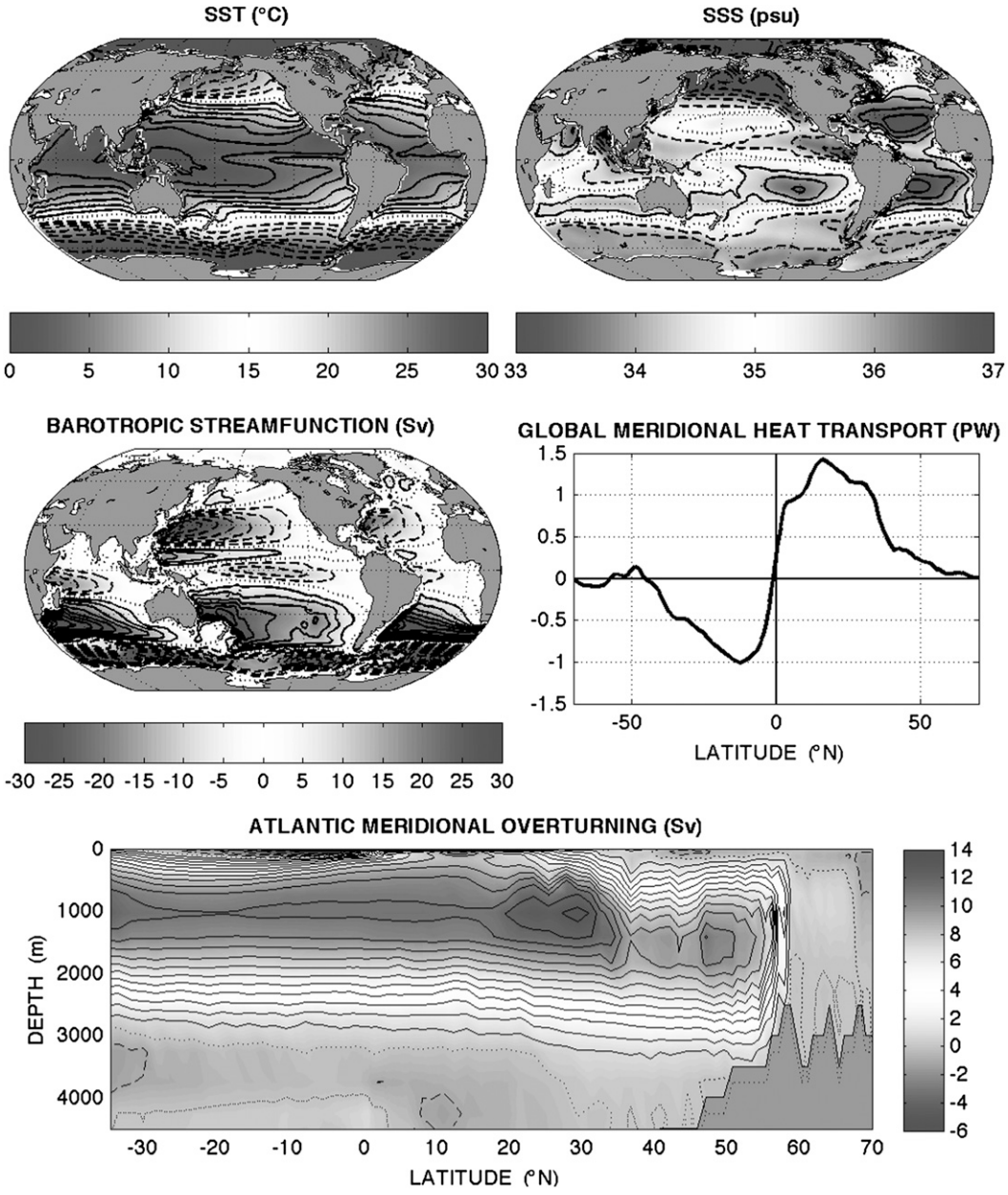

FIG. 1. The mean state of the ocean as reproduced by the full GCM. (top left) Sea surface temperature: contour intervals (CI) are 2°C; the dotted line corresponds to 15°C; and the solid and dashed lines correspond to higher and lower values, respectively. (top right) Sea surface salinity: CI are 0.5 psu; the dotted line corresponds to 35 psu; and the solid and dashed lines correspond to higher and lower values, respectively. (middle left) Barotropic streamfunction: CI are 5 Sv. (middle right) The global ocean meridional heat transport as a function of latitude. (bottom) Zonally averaged streamfunction for the Atlantic meridional overturning circulation: CI are 1 Sv. In the two streamfunction plots, solid, dashed, and dotted lines indicate positive, negative, and zero values. Seasonal variations are not shown.

$$|\mathbf{v}(t_f)\rangle = \mathbf{H}(t_f, t_i)|\mathbf{v}(t_i)\rangle\,, \tag{3}$$

where $\mathbf{H}(t_f, t_i)$ is called the propagator of the linearized dynamics from t_i to t_f.

The goal of the subsequent analysis is to assess the discrepancy between the model output and the observed ocean data but only for the temperature and salinity fields (not velocity); therefore, we will need to reduce

TABLE 1. Notations for the main vectors and operators.

$\|\mathbf{V}\rangle$	Ocean state vector consisting of all prognostic variables
$\langle \mathbf{V} \mid \mathbf{V}\rangle$	Norm of $\|\mathbf{V}\rangle$ based on the Euclidian scalar product
$\|\overline{\mathbf{V}}\rangle$	Nonlinear annual trajectory of $\|\mathbf{V}\rangle$
$\|\mathbf{v}\rangle$	Perturbation of $\|\mathbf{V}\rangle$
$\mathcal{N}$	Full time-dependent nonlinear operator of the ocean GCM
$\mathbf{A}(t)$	Jacobian matrix of $\mathcal{N}$
$\mathbf{H}(t_f, t_i)$	Linear propagator of $\|\mathbf{v}\rangle$ from time t_i to t_f
$\|\mathbf{U}\rangle$	Temperature and salinity component of $\|\mathbf{V}\rangle$
$\|\overline{\mathbf{U}}\rangle$	Nonlinear annual trajectory of $\|\mathbf{U}\rangle$
$\|\mathbf{u}\rangle$	Perturbation of $\|\mathbf{U}\rangle$
$\mathbf{P}$	Projector from $\|\mathbf{U}\rangle$ to $\|\mathbf{V}\rangle$
$\mathbf{M}(t_f, t_i)$	Linear propagator of $\|\mathbf{u}\rangle$ from time t_i to t_f
$\|\mathbf{U}_D\rangle$	Temperature and salinity fields as given by the Levitus dataset
$\mathbf{S}$	Operator of the thermohaline norm

the working parameter space. To do so, we define $|\mathbf{U}\rangle$ such that $|\mathbf{V}\rangle = \mathbf{P}|\mathbf{U}\rangle$, where $\mathbf{P}$ is the projector between the thermohaline (temperature–salinity) subspace, represented by $|\mathbf{U}\rangle$, and $|\mathbf{V}\rangle$. Then, (3) can be rewritten as

$$|\mathbf{u}(t_f)\rangle = \mathbf{M}(t_f, t_i)|\mathbf{u}(t_i)\rangle, \quad \mathbf{M}(t_f, t_i) = \mathbf{P}^{\dagger}\mathbf{H}(t_f, t_i)\mathbf{P}, \tag{4}$$

where $|\mathbf{u}\rangle$ is a perturbation in the thermohaline subspace such that $|\mathbf{v}\rangle = \mathbf{P}|\mathbf{u}\rangle$ and the dagger indicates an adjoint operator defined through the Euclidian norm.

In this last relation, there is no approximation involved. In the ocean GCM the prognostic variables are temperature, salinity, zonal and meridional velocities, and barotropic pressure (since the rigid-lid approximation is used). They are 3D fields, except for barotropic pressure, which is 2D. Together, these variables constitute the full state vector of the ocean. All of these variables are used in time integrations of the models we consider, including the full nonlinear model as well as its tangent linear and adjoint versions. However, we restrict optimal initial perturbations to temperature and salinity fields. Accordingly, the role of the projector $\mathbf{P}$ is to take the full ocean state vector and reduce it to a vector having only temperature and salinity fields as the vector components.

a. Method

In general, the model error is defined as the discrepancy (space and time dependent) between the observed ocean temperature and salinity fields $|\mathbf{U}_D\rangle$ given by the Levitus dataset, for instance (Levitus 1989), and the temperature and salinity output of the model at a given time $|\overline{\mathbf{U}}\rangle$ (where $|\overline{\mathbf{V}}\rangle = \mathbf{P}|\overline{\mathbf{U}}\rangle$): error $= |\mathbf{U}_D - \overline{\mathbf{U}}\rangle$.

For example, for 31 December, the difference between our ocean GCM output and the observed climatological field is characterized by pronounced temperature and salinity anomalies reaching ± 5°C and ± 1 psu in the upper ocean (Fig. 2). The temperature anomalies make SSTs in the Southern Hemisphere colder and in the Northern Hemisphere warmer than the observed climatology. If averaged over the top 1200 m, these anomalies show a strong warming in the Indian Ocean and the Gulf Stream region and a moderate cooling in the rest of the Atlantic.

The surface salinity field exhibits a strong bias along the intertropical convergence zone (ITCZ) and in high latitudes. At depths around 1000 m, a low-salinity anomaly develops in the Atlantic basin, most likely due to deficiencies in simulating the outflow of Mediterranean Water. For both temperature and salinity the bias is weak in the deep ocean (below 1500 m), with the exception of a moderate cooling in the Southern Ocean.

To measure the model error, we can use the ''distance'' between the actual model trajectory and the trajectory given by the climatological seasonal cycle,

$$\|\text{error}\| = \langle \mathbf{U}_D - \overline{\mathbf{U}}|\mathbf{S}|\mathbf{U}_D - \overline{\mathbf{U}}\rangle,$$

where $\mathbf{S}$ is a density-related, thermohaline norm defined as

$$\langle \mathbf{U}|\mathbf{S}|\mathbf{U}\rangle = \rho_0^2 \int\int\int \frac{\alpha^2 T^2 + \beta^2 S^2}{V}\, dv.$$

Here, T and S are the temperature and salinity components of the full state vector; ρ_0 is a reference density of seawater; α is the thermal expansion coefficient; β is the haline contraction coefficient; and V and dv are the full and unit ocean volumes, respectively.

As will become clear from (7) and (8), in general the choice of the norm can influence the results, especially if one chooses to put weights on contributions from particular regions or depths of the oceans. In other words, where and how you measure the data–model error will have an impact on how you reduce the error. Here, our approach is to select a norm that depends not on the location of the error but on the overall effect of error on the density field. Thus, we do not a priori discriminate against any particular regions of the ocean.

Further, a measure of the model bias is obtained by averaging $\|\text{error}\|$ over a chosen time interval,

$$\|\text{bias}\| = \frac{1}{t_2 - t_1}\int_{t_1}^{t_2} dt \langle \mathbf{U}_D - \overline{\mathbf{U}}|\mathbf{S}|\mathbf{U}_D - \overline{\mathbf{U}}\rangle, \tag{5}$$

where t_1 and t_2 are the limits of the time interval. Note that $\|\cdot\|$ in this expression indicates not a norm operator but an integral of a norm (still positive definite). Hereafter,

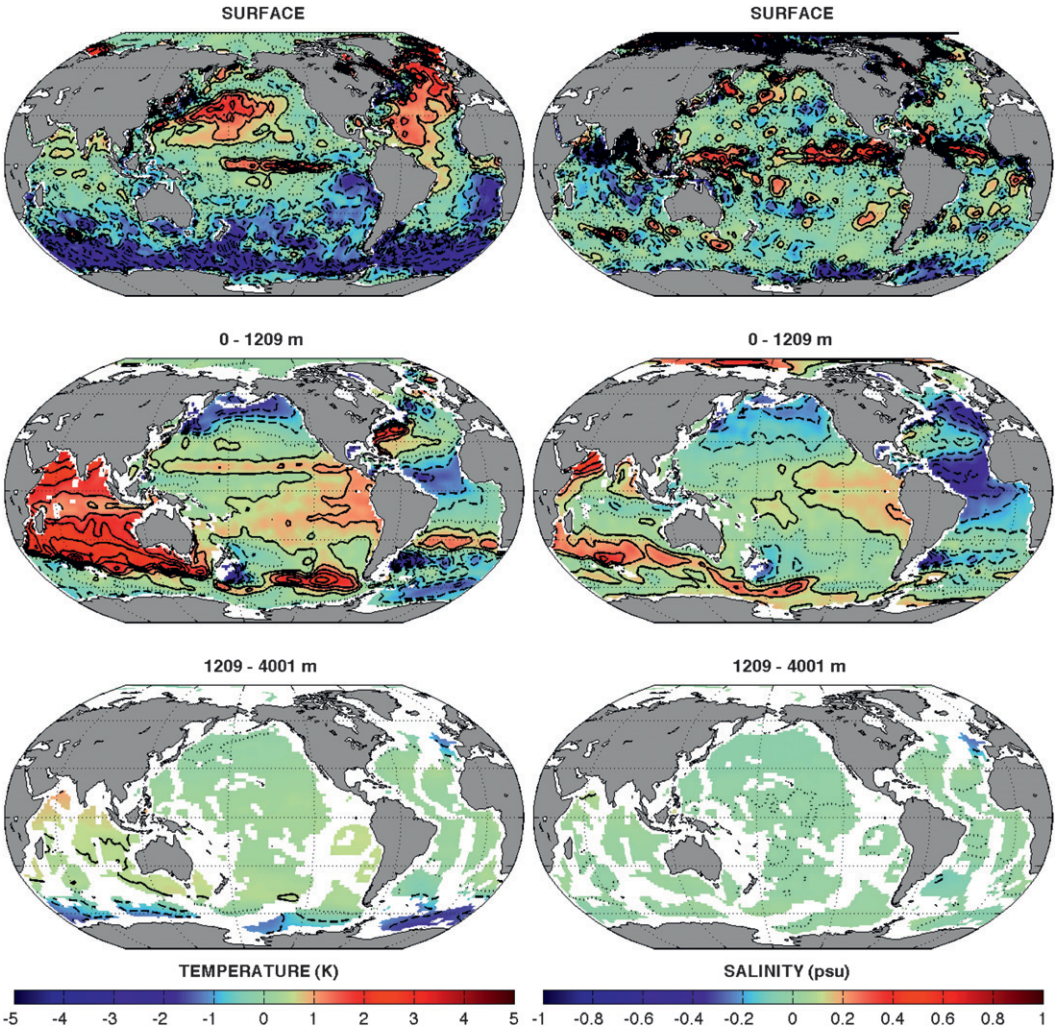

FIG. 2. The bias of the ocean GCM defined as the discrepancy between the observed climatological mean data (from the Levitus dataset) and the model simulations for (left) temperature and (right) salinity for 31 Dec. (top)–(bottom) Surface values and values averaged for the upper and deep ocean.

we will also refer to the full expression in (5) as the model bias.

Next, we will attempt to reduce the model bias over the duration of a chosen time interval by slightly modifying the initial conditions used for model initialization (Fig. 3). That is, we will look for the optimal initial perturbations (applied at time t_0) that will reduce the bias most efficiently over some future time interval (t_1 to t_2). This time interval could be the full model trajectory ($t_1 = t_0$ and $t_2 \to \infty$), a single snapshot ($t_1 \to t_2$), or any other combination of t_1 and t_2 such that $t_1 < t_2$. The reduction of the bias is evaluated by (5).

Obviously, in the limit $t_0 \ll t_1$ and $t_2 \to \infty$, the bias will not be affected, since the impact of initial perturbations is felt only for a limited amount of time if the system is asymptotically stable (Sévellec and Fedorov 2010, 2013a, 2013b, manuscript submitted to *Prog. Oceanogr.*). However, as we will demonstrate, for a reasonable choice of the time interval relevant for climate prediction, the bias can be effectively reduced.

Note that our approach has analogies to those data assimilation studies using adjoint methods in which the ocean state is adjusted at each time step of numerical simulations in order to reduce the difference between the simulated ocean state and the observations (e.g., Carton et al. 2000). However, in our study we modify only the initial conditions and only once, and then we assess the bias at a time interval one or two decades in the future.

In summary, we will minimize the bias, as measured by (5), by perturbing the model state vector via optimal initial perturbations (Fig. 3). Mathematically the problem can be formulated as

$$\|\text{bias}_{\text{pert}}\| \to 0 \Leftrightarrow \frac{1}{t_2 - t_1}\int_{t_1}^{t_2} dt\langle \mathbf{U}_D - (\overline{\mathbf{U}} + \mathbf{u})|\mathbf{S}|\mathbf{U}_D - (\overline{\mathbf{U}} + \mathbf{u})\rangle \to 0,$$

$$\Leftrightarrow \frac{1}{t_2 - t_1}\int_{t_1}^{t_2} dt\langle \mathbf{U}_D - \overline{\mathbf{U}}|\mathbf{S}|\mathbf{U}_D - \overline{\mathbf{U}}\rangle - \frac{2}{t_2 - t_1}\int_{t_1}^{t_2} dt\langle \mathbf{U}_D - \overline{\mathbf{U}}|\mathbf{S}|\mathbf{u}\rangle + \frac{1}{t_2 - t_1}\int_{t_1}^{t_2} dt\langle \mathbf{u}|\mathbf{S}|\mathbf{u}\rangle \to 0,$$

$$\Leftrightarrow \|\text{bias}\| - 2\frac{1}{t_2 - t_1}\int_{t_1}^{t_2} dt\langle \mathbf{U}_D - \overline{\mathbf{U}}|\mathbf{S}|\mathbf{u}\rangle + O(\mathbf{u}^2) \to 0.$$

At first, we assume that the last, second-order term in this expression is negligible and to modify the bias we will need to vary only $\langle \mathbf{U}_D - \overline{\mathbf{U}}|\mathbf{S}|\mathbf{u}\rangle$. Therefore, we obtain

$$\|\text{bias}_{\text{pert}}\| \to 0 \Leftrightarrow \max_{|\mathbf{u}\rangle}\left(\frac{1}{t_2 - t_1}\int_{t_1}^{t_2} dt\langle \mathbf{U}_D - \overline{\mathbf{U}}|\mathbf{S}|\mathbf{u}\rangle\right).$$

This last relation implies that reducing the bias requires adding to the model trajectory a perturbation (Fig. 3) that would have the largest projection onto the bias. Thus, we can reformulate the problem as a maximization problem; we will search for the initial perturbations that generate anomalies with the largest projection onto the bias.

The cost function of this maximization problem is then

$$f(t_1, t_2) = \frac{1}{t_2 - t_1}\int_{t_1}^{t_2} dt\langle \mathbf{U}_D - \overline{\mathbf{U}}|\mathbf{S}|\mathbf{u}\rangle. \tag{6}$$

We emphasize that, in our study, the cost function emerges as a direct consequence of the data–model discrepancy formulation and is not chosen subjectively or arbitrarily.

We now define a Lagrangian function that will be used to maximize the cost function with a normalization constraint for the initial perturbation $\langle \mathbf{u}(t_0)|\mathbf{S}|\mathbf{u}(t_0)\rangle = c^2$, where c is a normalization constant that gives the intensity of the initial perturbation,

$$\mathcal{L}(t_0, t_1, t_2) = \frac{1}{t_2 - t_1}\int_{t_1}^{t_2} dt\langle \mathbf{U}_D - \overline{\mathbf{U}}|\mathbf{S}|\mathbf{u}(t)\rangle - \gamma[\langle \mathbf{u}(t_0)|\mathbf{S}|\mathbf{u}(t_0)\rangle - c^2].$$

Here, γ is a Lagrange multiplier and the solution of the maximization problem is given by the condition $d\mathcal{L}(t_0, t_1, t_2) = 0$. Applying this condition, we find that the initial perturbation $|\mathbf{u}_{\text{opt}}^{\{t_1,t_2\}}(t_0)\rangle$ that maximizes $\int_{t_1}^{t_2} dt\langle \mathbf{U}_D - \overline{\mathbf{U}}|\mathbf{u}(t)\rangle$ is given by an explicit formula

$$|\mathbf{u}_{\text{opt}}^{\{t_1,t_2\}}(t_0)\rangle = \frac{c\int_{t_1}^{t_2} dt\mathbf{S}^{-1}\mathbf{M}^{\dagger}(t_0, t)\mathbf{S}|\mathbf{U}_D - \overline{\mathbf{U}}\rangle}{\left[\int\int_{t_1}^{t_2} dt\, dt'\langle \mathbf{U}_D - \overline{\mathbf{U}}|\mathbf{S}\mathbf{M}(t_0, t)\mathbf{S}^{-1}\mathbf{M}^{\dagger}(t_0, t')\mathbf{S}|\mathbf{U}_D - \overline{\mathbf{U}}\rangle\right]^{1/2}}, \tag{7}$$

where $\mathbf{M}^{\dagger}(t_1, t_2)$ is an adjoint operator (defined through the Euclidian scalar product) to the propagator $\mathbf{M}(t_2, t_1)$. Correspondingly, the bias reduction induced by the optimal initial perturbation can be calculated as

$$f(t_0, t_1, t_2) = \frac{c}{t_2 - t_1}\int_{t_1}^{t_2} dt\langle \mathbf{U}_D - \overline{\mathbf{U}}|\mathbf{S}\mathbf{M}(t, t_0)|\mathbf{u}_{\text{opt}}\rangle,$$

$$= \frac{c}{t_2 - t_1}\left[\int\int_{t_1}^{t_2} dt\, dt'\langle \mathbf{U}_D - \overline{\mathbf{U}}|\mathbf{S}\mathbf{M}(t_0, t)\mathbf{S}^{-1}\mathbf{M}^{\dagger}(t_0, t')\mathbf{S}|\mathbf{U}_D - \overline{\mathbf{U}}\rangle\right]^{1/2}. \tag{8}$$

For simplicity, the subsequent analysis will be confined to the limit $t_2 \to t_1$. That is, the averaging interval becomes an instance at a particular time t_1, or a snapshot. Then, (7) and (8) can be simplified to

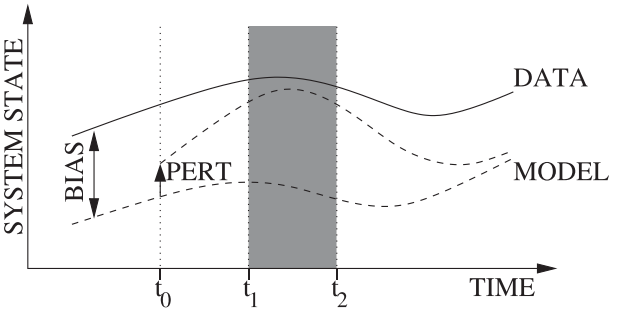

FIG. 3. A schematic of our approach. Observed and simulated trajectories of the ocean state vector are represented by solid (data) and dashed (model) lines, respectively. A systematic discrepancy between the model and data trajectories results in the model bias. An optimal initial perturbation (arrow) is applied at time t_0 to the model trajectory to reduce the bias over a time interval between t_1 and t_2 (shaded gray). The dashed line that starts from the arrow represents the perturbed trajectory of the model. The new, reduced bias is estimated as the distance between the perturbed model trajectory and the observational trajectory over the same time interval. Time progression along the horizontal axis corresponds to decadal changes.

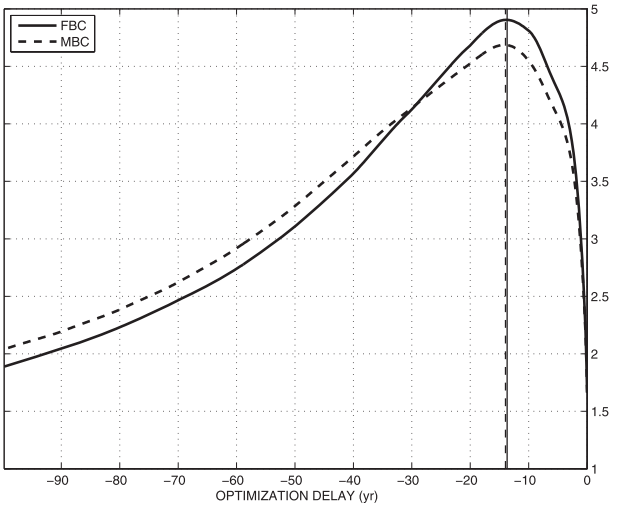

FIG. 4. Maximum increase in the cost function [see (10)] as a function of the chosen optimization delay. Solid and dashed lines correspond to calculations with the flux and mixed boundary conditions, respectively. For both types of experiments, there exists an optimal (most efficient) delay at around 14 yr (indicated by solid and dashed vertical lines). This particular delay yields the strongest increase in the cost function and hence the strongest reduction of the model bias (for a fixed amplitude of initial perturbations).

$$|\mathbf{u}^{\tau}_{\mathrm{opt}}(\tau)\rangle = c\,\frac{\mathbf{S}^{-1}\mathbf{M}^{\dagger}(\tau)\mathbf{S}|\mathbf{U}_D - \overline{\mathbf{U}}\rangle}{[\langle \mathbf{U}_D - \overline{\mathbf{U}}|\mathbf{S}\mathbf{M}(-\tau)\mathbf{S}^{-1}\mathbf{M}^{\dagger}(\tau)\mathbf{S}|\mathbf{U}_D - \overline{\mathbf{U}}\rangle]^{1/2}}, \tag{9}$$

$$f(\tau) = c[\langle \mathbf{U}_D - \overline{\mathbf{U}}|\mathbf{S}\mathbf{M}(-\tau)\mathbf{S}^{-1}\mathbf{M}^{\dagger}(\tau)\mathbf{S}|\mathbf{U}_D - \overline{\mathbf{U}}\rangle]^{1/2}, \tag{10}$$

where we set $t_0 = \tau$ as the time of model initialization (τ is the maximization delay) and $t_1 = 0$ as the time when we assess the bias. Note that, although in this simplified approach we aim to minimize the model bias at t_1, effectively the bias will be reduced for a decade or so around this time (Fig. 3).

b. Results

Next, we will analyze in detail the spatial structure and the ensuing impacts of the initial perturbations given by (9) and (10). Calculations are conducted for two types of surface boundary conditions: the mixed boundary conditions (MBC; surface restoring for temperature and a constant flux for salinity) and the flux boundary conditions (FBC; constant fluxes for both temperature and salinity).

We have tested different τ, ranging from 0 to 100 yr, and found that the timing of the initial perturbations is critical for how much the data–model discrepancy is reduced (Fig. 4). In fact, for both types of the boundary conditions there exists an optimal delay ($\tau_{\mathrm{opt}} = -13.7$ and -14.0 yr for FBC and MBC, respectively). The initial perturbations computed for this particular delay will cause the strongest possible reduction of the data–model discrepancy after the delay. The magnitude of the reduction depends little on the type of the boundary conditions (with only a 4.5% difference; Fig. 4), which confirms the robustness of our results. This is because the damping introduced by the surface restoring term acts only on the top model level (10 m) and is negligible, in the context of bias reduction, as compared to other processes integrated over the full ocean depth.

The structure of the optimal initial perturbations is characterized by temperature and salinity anomalies especially pronounced at depth in the Southern Ocean. At intermediate depths, initial temperature anomalies in the Indian Ocean and salinity anomalies in the Atlantic are also notable (Fig. 5). Anomalies at the ocean surface are generally much weaker. Overall, initial temperature and salinity anomalies have a constructive effect on density (i.e., warm temperature anomalies coincide with low salinity anomalies) for both FBC and MBC experiments. Because we apply a restoring term for MBC at the surface, near-surface anomalies are weaker in this case than for FBC. However, since the optimal initial perturbations occupy a thick layer of the deep ocean, the FBC and MBC experiments exhibit only minor differences overall.

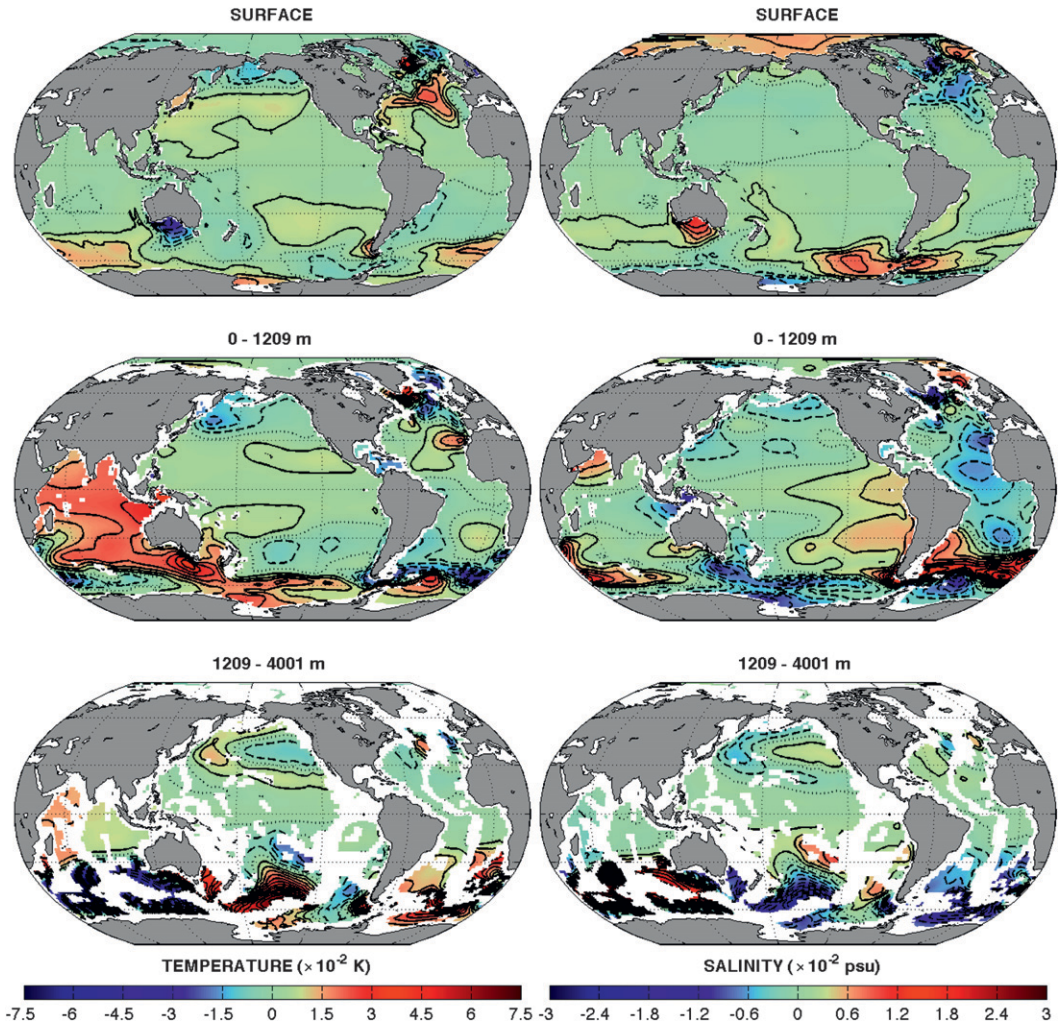

FIG. 5. The spatial structure of (left) temperature and (right) salinity fields of the optimal initial perturbation in the experiments with the flux boundary conditions. (top)–(bottom) Surface values and values averaged for the upper and deep oceans. For the normalization constant in the Lagrangian, we used $c = 7.5 \times 10^{-3}$ kg m^{-3}, which would give a 10% reduction of the bias within the weakly nonlinear approach (see section 3c).

As expected, initializing the linear model using the optimal perturbations leads to a gradual increase of the cost function (Fig. 6, left) and the corresponding decrease of the bias. The cost-function increase is associated with the transient increase of the thermohaline norm $\langle \mathbf{u}(t)|\mathbf{S}|\mathbf{u}(t)\rangle$ by factors of 87 and 77 for the FBC and MBC experiments, respectively (Fig. 6, right). Such an increase of the thermohaline norm is a typical consequence of the nonnormality of the transient change ($\mathbf{AA}^{\dagger} - \mathbf{A}^{\dagger}\mathbf{A} \neq 0$) and indicates the growth of the initial disturbances.

At the time of the maximum impact, the optimal perturbations induce temperature and salinity anomalies localized primarily in the top 1000 m of the Southern Ocean and, to a lesser degree, the Atlantic Ocean (Fig. 7 for FBC; not shown for MBC). The anomalies are now temperature dominated with a partial compensation from salinity. This is different from the initial perturbations having constructive effects of temperature and salinity on density (this difference between the initial and fully developed anomalies is another signature of the nonnormality of the transient change).

The main difference between the FBC and MBC experiments is the vanishing of temperature anomalies in the upper 10 m for the MBC case, caused by the temperature restoring at the surface. Another difference is weaker anomalies in the North Atlantic for MBC, which is related to the damping of interdecadal AMOC variations in the presence of surface restoring (Huck and Vallis 2001; Arzel et al. 2006; Sévellec et al. 2009;

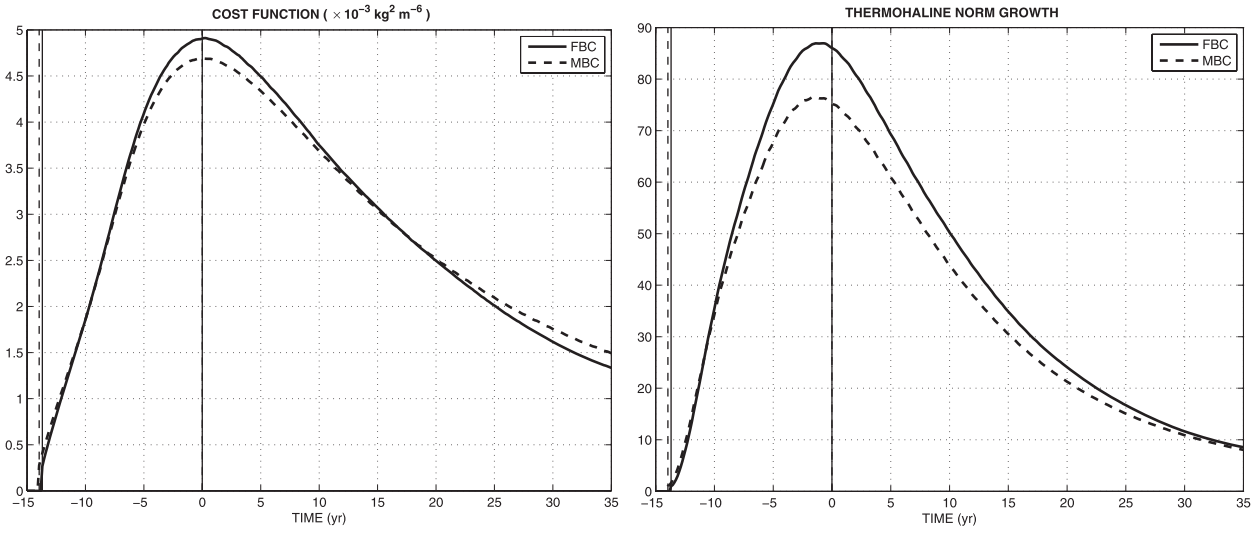

FIG. 6. (left) Temporal evolution of the cost function in the GCM calculations after the optimal initial perturbation was applied. The strongest increase in the cost function corresponds to the strongest reduction in the bias. (right) The relative increase of the thermohaline (temperature–salinity) norm for the optimal perturbation, defined as $\langle \mathbf{u}_{\text{opt}}^{\tau_{\text{opt}}}(t)|\mathbf{S}|\mathbf{u}_{\text{opt}}^{\tau_{\text{opt}}}(t)\rangle/\langle \mathbf{u}_{\text{opt}}^{\tau_{\text{opt}}}(0)|\mathbf{S}|\mathbf{u}_{\text{opt}}^{\tau_{\text{opt}}}(0)\rangle$, during the same time integrations. The spatial structure and amplitude of the initial perturbation were shown in Fig. 5.

Sévellec and Fedorov 2013b, manuscript submitted to *Prog. Oceanogr.*). However, the overall impacts on the data–model discrepancy are similar for FBC and MBC (with only a 4.5% difference in Fig. 6, left).

The intensification of the ocean response in the upper ocean (14 yr or so after initialization) results from the efficient projection of the initial perturbations onto the model bias. Accordingly, although the initial perturbations are largely confined to the deep ocean, the ocean response is amplified in the upper ocean. An optimal initial perturbation smaller than 0.1 K in the deep ocean (Fig. 5, bottom left) can lead to a subsequent anomaly of several kelvins in the upper ocean (Fig. 7, top left and middle left).

The aforementioned effects stem from the nonnormality of ocean dynamics and have major implications for ocean dynamics and predictability that go beyond our original intent to reduce data–model discrepancy. In fact, a corollary of these results is that small errors in model initialization in the deep ocean (especially in the Southern Ocean) can grow significantly and induce large anomalies in the upper ocean after a little more than a decade. While so far we have chosen initial perturbations specifically to reduce the data–model discrepancy, similar initial perturbations could actually increase this discrepancy. In fact, within the linear approximation, simply taking the same perturbations but with the opposite sign would do just that. This result implies a potential predictability barrier set solely by ocean dynamics [also see Sévellec and Fedorov (2010)].

c. The role of nonlinearity

As derived previously, the full model bias (after the initial perturbation was applied) can be computed as

$$\|\text{bias}_{\text{pert}}\| = \langle \mathbf{U}_D - \overline{\mathbf{U}}|\mathbf{S}|\mathbf{U}_D - \overline{\mathbf{U}}\rangle - 2\langle \mathbf{U}_D - \overline{\mathbf{U}}|\mathbf{S}|\mathbf{u}\rangle + \langle \mathbf{u}|\mathbf{S}|\mathbf{u}\rangle . \quad (11)$$

In this section, we will study the role of the intensity of the initial perturbation, given by the amplitude c in (9) and (10), and thus assess the role of nonlinearity in (11).

As expected, the bias calculated from the linear expression [i.e., neglecting the second-order term in (11)] reduces in proportion to the strength of the initial perturbation (Fig. 8, solid line). An initial anomaly of about 1 K would erase the bias completely. However, as the subsequent analysis shows, nonlinearity becomes important already for the strength of initial perturbations on the order of 0.2 K, which limits the applicability of the linear approach.

To test the importance of nonlinearity in (11), we retain the second-order term $\langle \mathbf{u}|\mathbf{S}|\mathbf{u}\rangle$ and at first estimate it using (9) obtained in the linear context. As evident from (11), the second-order term always increases the model–data discrepancy (because $\langle \mathbf{u}|\mathbf{S}|\mathbf{u}\rangle > 0$). As a result, the maximum reduction of this estimated weakly nonlinear bias does not exceed 15%, which is achieved for the strength of the initial perturbation of about 0.3 K (Fig. 8, dashed line). This corresponds to the optimal value of c in the weakly nonlinear context. This value can be obtained by substituting (9) into (11) and finding the minimum ($\partial_c\|\text{bias}_{\text{pert}}\| = 0$),

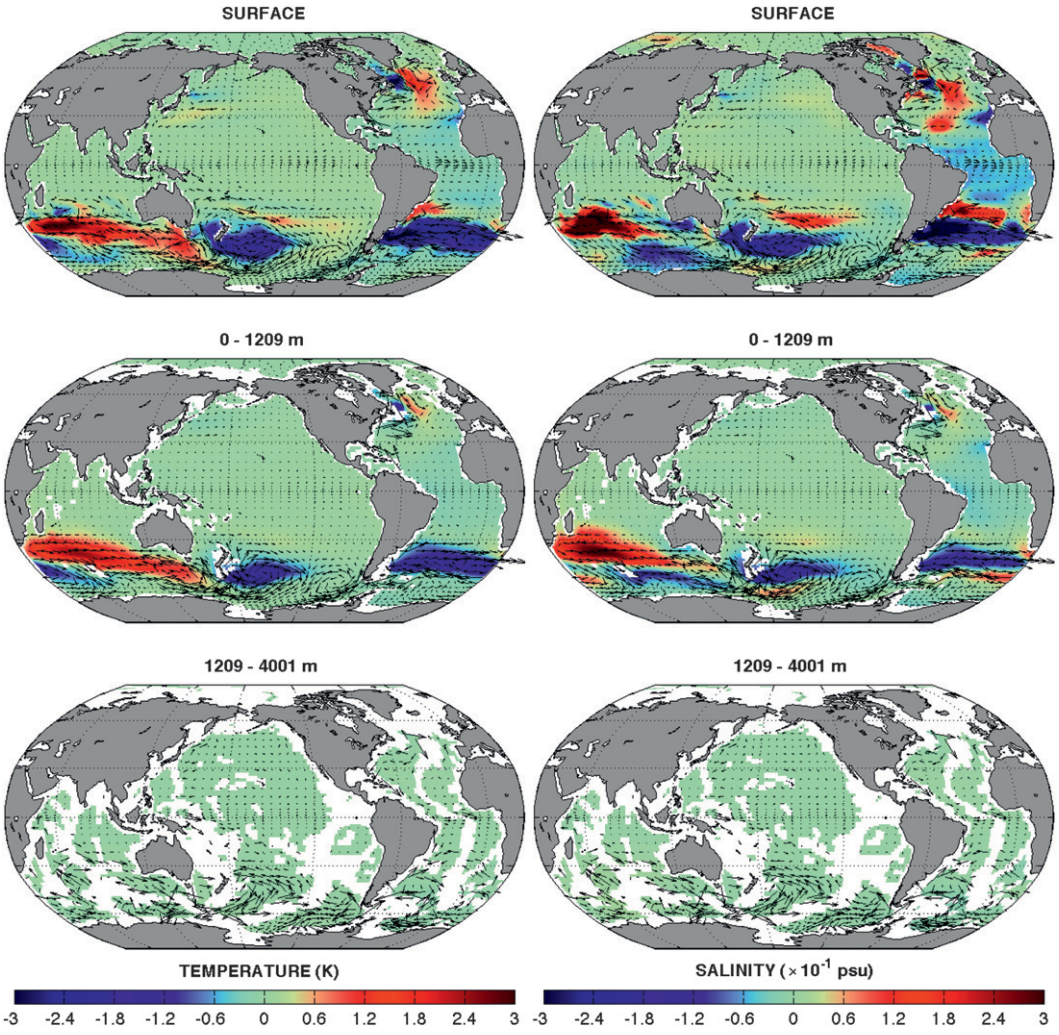

FIG. 7. Anomalies in (left) temperature and (right) salinity induced by the optimal initial perturbation at the moment of the maximum increase of the cost function (13.7 yr after initialization; see Fig. 6) for the experiments with the flux boundary conditions. Arrows represent oceanic horizontal velocities. (top)–(bottom) Surface values and values averaged for the upper and deep oceans. The spatial structure and amplitude of the initial perturbation are shown in Fig. 5.

$$c_{\mathrm{opt}} = \frac{\langle \mathbf{U}_D - \overline{\mathbf{U}} | \mathbf{SM}(-\tau_{\mathrm{opt}}) \mathbf{S}^{-1} \mathbf{M}^{\dagger}(\tau_{\mathrm{opt}}) \mathbf{S} | \mathbf{U}_D - \overline{\mathbf{U}} \rangle^{3/2}}{\langle \mathbf{U}_D - \overline{\mathbf{U}} | \mathbf{SM}(-\tau_{\mathrm{opt}}) \mathbf{S}^{-1} \mathbf{M}^{\dagger}(\tau_{\mathrm{opt}}) \mathbf{SM}(-\tau_{\mathrm{opt}}) \mathbf{S}^{-1} \mathbf{M}^{\dagger}(\tau_{\mathrm{opt}}) \mathbf{S} | \mathbf{U}_D - \overline{\mathbf{U}} \rangle}. \tag{12}$$

Numerical computations yield $c_{\mathrm{opt}} \simeq 7.5 \times 10^{-3}$ kg m^{-3}.

Next, to increase the accuracy of calculations we repeat our analysis and minimize both the first-order term in (11) and the second-order correction to the bias (as described in details in the appendix). This procedure involves expanding $|\mathbf{u}\rangle$ while using the magnitude of the initial anomaly as the expansion parameter. The maximum reduction of the bias obtained by this approach (Fig. 8, solid gray line) reaches about 10% for the strength of the initial anomaly of about 0.18 K, which is not much different from the reduction that the linear approach would have given for initial anomalies of the same magnitude.

On the whole, the expansion procedure suggests that initial amplitudes of 0.1–0.2 K set the limit of applicability for the linear or weakly nonlinear approaches. Apparently, for greater amplitudes the expansion method does not converge and, in order to reduce the bias further,

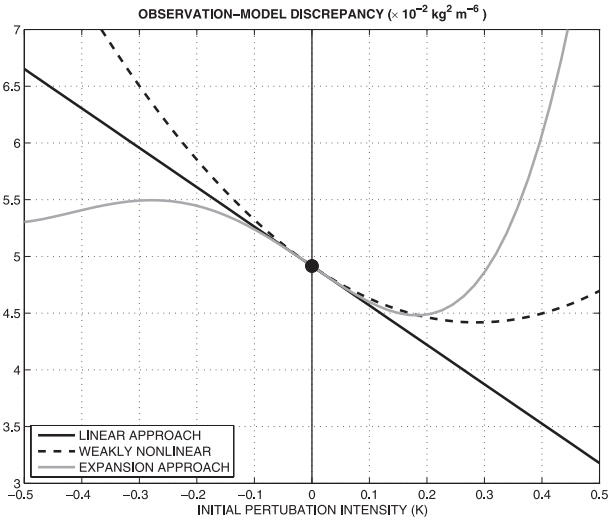

FIG. 8. Observation–model discrepancy (model bias) at the time of the maximum impact of the optimal initial perturbation as a function of perturbation intensity as estimated by different approaches, for the experiments with the flux boundary conditions. The black solid and dashed lines show the discrepancy following (11), given by the linear and weakly nonlinear approximations, respectively. The gray line shows the result obtained by the proper expansion procedure while neglecting third- and higher-order terms [see (A1)]. The discrepancy is measured as the distance between the observations and the model output and is given by the thermohaline norm. The black dot shows this discrepancy in the absence of initial perturbations. The intensity of the initial perturbations is defined as the maximum of the corresponding temperature anomaly. The plot shows that the three methods yield similar results for initial perturbations with amplitudes below 0.15–0.2 K, resulting in a bias reduction of 10%–15%. For higher amplitudes, however, these methods diverge and a fully nonlinear approach is required.

one would need to use a fully nonlinear approach rather than a perturbation expansion. This could be done, for example, by computing conditional nonlinear optimal perturbations (e.g., Mu et al. 2004; Mu and Zhang 2006; Mu et al. 2007), but this method is not yet extensively developed for the use with ocean GCMs.

4. Idealized model

a. Main assumptions and equations

Next, we will formulate an idealized ocean model (Fig. 9) to highlight the fundamental mechanism of the transient change and its nonnormal characteristics within the linear approach. The setting of the idealized model follows that of Sévellec and Fedorov (2013a) and Sévellec and Fedorov (2013b, manuscript submitted to *Prog. Oceanogr.*) and is designed to replicate the dynamics of the linear tangent and adjoint versions of the ocean GCM with the flux boundary conditions.

There are several simplifying approximations used in the idealized model. First, concentrating on the decadal

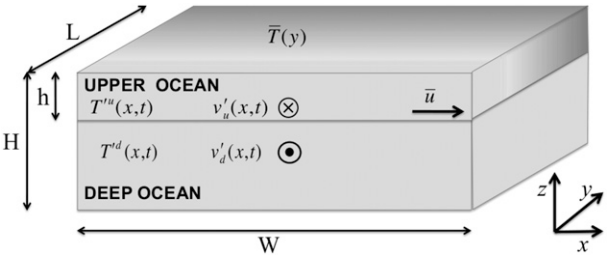

FIG. 9. A schematic of the idealized model. The upper and deep oceans are represented by two model levels (or layers). Zonal periodicity is assumed and salinity is neglected. The model prognostic variables are temperatures in the upper and deep oceans (T'^u and T'^d, respectively). The diagnostic variables are meridional velocities, also in the upper and deep oceans (v'_u, and v'_d, respectively). The main model parameters are the upper-ocean thickness h; the total ocean depth H; the zonal and meridional extent of the Southern Ocean basin (W and L, respectively), the mean zonal velocity in the upper ocean $\overline{u}$; and the mean temperature field in the upper ocean $\overline{T} = \overline{T}(y)$. The intensity of shading (lighter to darker) represents meridional variations in the mean temperature (colder to warmer). In the upper ocean, we assume that the mean temperature is a linear function of y. In the deep ocean, we use a constant value equal to the temperature at the southern basin boundary in the upper ocean. The dependency of model variables from spatial coordinates (zonal x, meridional y, and vertical z) and time t is shown in parentheses.

time scales of the transient change, we treat the system as autonomous (no seasonal cycle). Second, we will consider only temperature anomalies (no salinity), since they dominate the optimal initial perturbations in the GCM. Finally, the large spatial scale of the problem allows us to reduce the model momentum equations to geostrophic balance on an f plane (i.e., the planetary-geostrophic regime; Colin de Verdière 1988).

The model describes anomalies in temperature T at two levels: the top level (of depth h, where ocean stratification is strong) and the deeper level (with weak or no stratification). These anomalies depend on time t and the zonal and meridional coordinates x and y, respectively. The configuration of the basin is chosen to represent the Southern Ocean as a zonal periodic channel with rigid boundaries at the north and south. The size of the channel in the zonal and meridional directions is W by L, respectively; the full ocean depth is H.

The model is linearized with respect to the mean state of the ocean. In particular, at the upper level we impose a mean zonal flow $\overline{u}$ (the other horizontal flow component being neglected) and a mean meridional temperature gradient $\partial_y \overline{T}$ (where $\overline{T}$ is the mean temperature). The mean zonal and vertical gradients of temperature within the upper layer are neglected. In the deeper layer, all mean temperature gradients and the mean flow are neglected. In the equations for the upper layer,

TABLE 2. Key parameters of the idealized model.

h	1000 m	Upper-ocean thickness
H	5000 m	Total ocean depth
W	360°	Zonal size of the basin
L	25°	Meridional size of the basin
κ	2×10^3 m^2 s^{-1}	Horizontal tracer diffusivity
g	9.8 m s^{-2}	Acceleration of gravity
f	-1.25×10^{-4} s^{-1}	Coriolis parameter
α	2×10^{-4} K^{-1}	Thermal expansion coefficient
ΔT	15 K	Meridional temperature contrast

the mean flow and mean temperature gradient are set to constants.

Temperature anomalies in the upper and deep oceans (T'^u and T'^d) are two prognostic variables of the model. They evolve according to linearized advective–diffusive equations with horizontal diffusivity κ,

$$\partial_t T'^u = -\overline{u}\partial_x T'^u - v'\partial_y \overline{T} + \partial_y(\kappa\partial_y T'^u) + \partial_x(\kappa\partial_x T'^d), \tag{13a}$$

$$\partial_t T'^d = \partial_y(\kappa\partial_y T'^d) + \partial_x(\kappa\partial_x T'^d). \tag{13b}$$

The system is closed using a linear equation of state for seawater and thermal-wind balance for the meridional velocity v supplemented with a baroclinicity condition,

$$\partial_z v = \frac{\alpha g}{f}\partial_x T \quad \text{with} \quad \int_{-H}^{0} dz\, v = 0, \tag{14}$$

where f is the Coriolis parameter, g is the acceleration of gravity, and α is the thermal expansion coefficient (for the particular values of these and others parameters, see Table 2). Applied to the two-level idealized model, this relation yields the upper level velocity v' as

$$v'_u = \frac{\alpha g\tilde{h}}{2Hf}(h\partial_x T'^u + \tilde{h}\partial_x T'^d),$$

where $\tilde{h} = H - h$ is the thickness of the deep layer. We also use periodicity in the zonal direction and the zero heat flux condition at the ocean surface and latitudinal boundaries (which corresponds to the FBC in the ocean GCM experiments).

We now apply the Fourier transform in x and y to T'^u and T'^d, which yields Fourier coefficients T'^u_{cnm}, T'^u_{snm}, T'^d_{cnm}, and T'^d_{snm} (where n and m are the zonal and meridional wavenumbers and c and s stand for cosine and sine),

$$T' = \sum_{n,m} T'_{cnm}\cos\left(\frac{n\pi}{W}x + \frac{m\pi}{L}y\right) + T'_{snm}\sin\left(\frac{n\pi}{W}x + \frac{m\pi}{L}y\right).$$

The resultant equations for these coefficients are

$$\begin{aligned}
d_t T'^u_{cnm} &= -\frac{n\pi}{W}\left[\frac{\alpha g\tilde{h}}{2Hf}\partial_y\overline{T}(hT'^u_{snm} + \tilde{h}T'^d_{snm}) + \overline{u}T'^u_{snm}\right] \\
&\quad - \kappa\left[\left(\frac{n\pi}{W}\right)^2 + \left(\frac{m\pi}{L}\right)^2\right]T'^u_{cnm}, \\
d_t T'^u_{snm} &= +\frac{n\pi}{W}\left[\frac{\alpha g\tilde{h}}{2Hf}\partial_y\overline{T}(hT'^u_{snm} + \tilde{h}T'^d_{snm}) + \overline{u}T'^u_{cnm}\right] \\
&\quad - \kappa\left[\left(\frac{n\pi}{W}\right)^2 + \left(\frac{m\pi}{L}\right)^2\right]T'^u_{snm}, \\
d_t T'^d_{cnm} &= -\kappa\left[\left(\frac{n\pi}{W}\right)^2 + \left(\frac{m\pi}{L}\right)^2\right]T'^d_{cnm}, \\
d_t T'^d_{snm} &= -\kappa\left[\left(\frac{n\pi}{W}\right)^2 + \left(\frac{m\pi}{L}\right)^2\right]T'^d_{snm}.
\end{aligned}$$

The zonal periodicity of the basin restricts the zonal wavenumbers to even numbers. We will restrict our treatment to the largest scale possible ($n = 2$ and $m = 1$; the other modes will be damped by horizontal diffusion).

In addition, we will make two other simplifying approximations. The first one is an assumption that $(\alpha g\tilde{h}h/2Hf)\partial_y\overline{T} + \overline{u} \simeq 0$. That is, the mean zonal flow in the upper layer is determined solely by the mean meridional temperature gradient. Such a cancellation of these two terms, which would be exact in the 1.5-layer shallow-water model, is known as the non-Doppler effect (Rossby 1939; Held 1983; Killworth et al. 1997). Note that, in a realistic system, the mean flow has barotropic as well as higher-mode baroclinic components, which can shift this balance significantly. By making this approximation we neglect the propagation of anomalies in the zonal direction and concentrate solely on their growth and interaction between the upper and deep ocean.

The second assumption is that the aspect ratio of the Southern Ocean is such that $W \gg L$, which allows us to neglect zonal diffusion for the large-scale mode. These two assumptions lead to a new, very much simplified system of equations,

$$d_t\begin{pmatrix} T'_u \\ T'_d \end{pmatrix} = \begin{bmatrix} -\kappa\left(\frac{\pi}{L}\right)^2 & \frac{2\pi}{W}\frac{\alpha g\tilde{h}^2}{2Hf}\partial_y\overline{T} \\ 0 & -\kappa\left(\frac{\pi}{L}\right)^2 \end{bmatrix}\begin{pmatrix} T'_u \\ T'_d \end{pmatrix}, \tag{15}$$

where T'_u and T'_d are the Fourier amplitudes of the temperature anomalies in the upper and deep oceans, respectively. These are the equations we will use in the subsequent analysis.

This system is degenerate and has only one eigenvalue $\lambda = -\kappa(\pi/L)^2$. A reasonable choice of parameters (Table 2) yields an e-folding decay scale of $\tau = 1/\lambda = -12.5$ yr for this eigenvalue. The corresponding eigenvector is $\langle \mathbf{e}| = (1, 0)$, which indicates that the eigenmode is confined to the upper ocean.

We can also obtain the biorthogonal $\langle \mathbf{e}^\dagger| = (0, 1)$. The biorthogonal vector is the eigenvector of the adjoint problem, and as such it controls the sensitivity of the eigenmode of the forward problem. Although the dynamics of the damped eigenmode $|\mathbf{e}\rangle$ is determined by the upper ocean, its sensitivity $|\mathbf{e}^\dagger\rangle$ is determined by the deep ocean. This is a clear sign of the nonnormality of the dynamics, $\mathbf{A}\mathbf{A}^\dagger - \mathbf{A}^\dagger\mathbf{A} \neq 0$, where $\mathbf{A}$ is the matrix used in (15). Next, will use this simple model to understand the main features of our GCM calculations and the transient change in particular.

b. Optimal perturbation analysis

As discussed previously, the discrepancy between the actual oceanic data and the GCM output is greatest in the upper ocean (the top 1000 m). Therefore, in the idealized model we assume that all potential bias is confined to the upper layer. Accordingly, analogously to (6), we define the cost function as $f(t) = \langle \mathbf{F}|\mathbf{u}(t)\rangle$, where $\langle \mathbf{F}| = (1, 0)$, and the norm as

$$\langle \mathbf{u}|\mathbf{S}|\mathbf{u}\rangle = \frac{h}{H} T_u'^2 + \frac{\tilde{h}}{H} T_d'^2 .$$

Using (9) and (10), we obtain that the optimal change of the cost function for this idealized model is

$$f(\tau) = \sqrt{\langle \mathbf{F}|\mathbf{M}(-\tau)\mathbf{S}^{-1}\mathbf{M}^\dagger(\tau)|\mathbf{F}\rangle},$$
$$= \sqrt{\frac{H}{h} e^{-2\kappa(\pi/L)^2\tau} + \frac{H}{\tilde{h}}\left(\frac{2\pi}{W}\frac{\alpha g \tilde{h}^2}{2Hf}\partial_y \overline{T}\tau\right)^2 e^{-2\kappa(\pi/L)^2\tau}}, \tag{16}$$

where $\mathbf{M}(-\tau) = \exp(-\mathbf{A}\tau)$ is the propagator of the idealized model and τ is the time delay for which we maximize the cost function. The corresponding initial perturbation is

$$|\mathbf{u}_0^\tau\rangle = \frac{e^{-\kappa(\pi/L)^2\tau}}{f(\tau)} \begin{pmatrix} \dfrac{H}{h} \\ \dfrac{2\pi}{W}\dfrac{\alpha g \tilde{h}}{2f}\partial_y \overline{T}\tau \end{pmatrix}. \tag{17}$$

This result indicates that indeed the optimal initial perturbations have the strongest signature in the deep ocean for sufficiently long τ (for τ sufficiently longer than the advective time scale of about 1 yr, see the bottom-left panel of Fig. 10). This agrees well with our GCM analysis.

Further, we find the optimal (most efficient) delay τ_{opt} from the condition $d_\tau f|_{\tau_{\text{opt}}} = 0$. This optimal time scale exists if diffusion is slower than the advection time scale and is given by the expression

$$\tau_{\text{opt}} = \frac{1 \pm \left\{1 - 4\dfrac{\tilde{h}}{h}\dfrac{\kappa^2(\pi/L)^4}{[(2\pi/W)(\alpha g \tilde{h}^2/2Hf)\partial_y \overline{T}]^2}\right\}^{1/2}}{2\kappa(\pi/L)^2}$$
$$\simeq \begin{cases} \dfrac{1}{\kappa(\pi/L)^2} . \\ 0 \end{cases} \tag{18}$$

For a reasonable choice of diffusivity and the basin meridional size (Table 2), we obtain $\tau_{\text{opt}} = 12.5$ yr or $\tau_{\text{opt}} = 17$ days. The latter time scale corresponds to the least efficient delay; however, it is too short to be considered given the approximations of our analysis. On the other hand, $\tau_{\text{opt}} = 12.5$ yr corresponds to the most efficient delay, as suggested by our numerical results (Fig. 10, top left) and is very close to the value produced by the ocean GCM.

Using the propagator matrix, we obtain the time evolution of the optimal perturbation $|\mathbf{u}_0^{\tau_{\text{opt}}}\rangle$ as

$$|\mathbf{u}_0^{\tau_{\text{opt}}}(t)\rangle = \mathbf{M}(t)|\mathbf{u}_0^{\tau_{\text{opt}}}\rangle = \frac{e^{-\kappa(\pi/L)^2\tau_{\text{opt}}}}{f(\tau_{\text{opt}})} \begin{bmatrix} \dfrac{H}{h} + \dfrac{H}{\tilde{h}}\left(\dfrac{2\pi}{W}\dfrac{\alpha g \tilde{h}^2}{2Hf}\partial_y \overline{T}\right)^2 \tau_{\text{opt}} t \\ \dfrac{2\pi}{W}\dfrac{\alpha g \tilde{h}}{2f}\partial_y \overline{T}\tau_{\text{opt}} \end{bmatrix} e^{-\kappa(\pi/L)^2 t}. \tag{19}$$

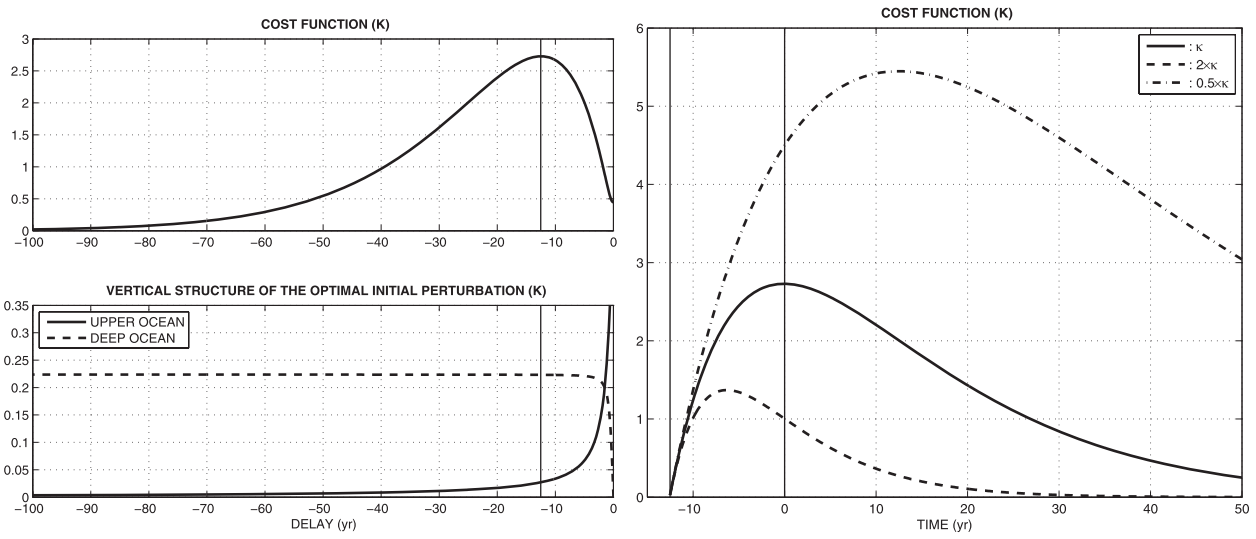

FIG. 10. (top left) The maximum transient increase in the cost function [see (16)] as a function of the optimization delay in the idealized model (cf. Fig. 4 for the ocean GCM). (bottom left) The vertical structure of the optimal initial perturbation, showing temperature anomalies at the model upper and deep levels, for different optimization delays. For delays longer than 1–2 yr, the optimal perturbation is located predominantly in the deep ocean. (right) Temporal evolution of the cost function after an optimal initial perturbation (corresponding to the most efficient delay of 12.5 yr) was applied in the idealized model, for the original and two other different values of horizontal diffusivity κ. The thick solid line describes the result obtained for the same diffusivity as used in the ocean GCM. The strongest increase in the cost function corresponds to the strongest reduction in the model bias. Note that in the idealized model the cost function is proportional to the temperature anomaly in the upper ocean. The vertical solid lines indicate the most optimal (most efficient) delay for the original κ.

This expression indicates that temperature in the upper ocean will exhibit a transient increase because of a secular term in the first component of the vector. The increase peaks at τ_{opt} (solid line in the right panel of Fig. 10). By contrast, the temperature anomaly in the deep ocean decays with an e-folding time scale $-L^2/(\pi^2\kappa)$ set by diffusion. Eventually, after the transient increase, the upper-ocean anomaly will decay at the same rate.

Using (16) and (18) we obtain the magnitude of the optimal transient change as

$$f(\tau_{\mathrm{opt}}) \simeq \frac{1}{\pi e}\frac{\tilde{h}^2}{\sqrt{H\tilde{h}}}\frac{L^2}{W}\frac{\alpha g}{\kappa f}\partial_y \overline{T}, \tag{20}$$

where we assumed that the advective time scale is much faster than the diffusive one. Thus, the magnitude of the upper-ocean response is proportional to the mean meridional gradient of temperature in the upper ocean, which confirms that the transient change is related to the existence of the meridional temperature gradient.

The transient change mechanism involves three main phases: 1) An optimal temperature anomaly in the deep ocean induces a geostrophic flow that affects the upper ocean via thermal wind balance. 2) The resulting upper-ocean flow interacts with the mean gradient of temperature, existing in the upper ocean, and induces a temperature anomaly there. This again emphasizes the role of the mean meridional temperature gradient in the upper ocean for the transient change. 3) The diffusion of the initial anomaly in the deep ocean slows down the process, and in due time both anomalies dissipate.

This analysis also points to the importance of horizontal diffusivity κ for the optimal change time scale [see (18)] and for the magnitude of the ocean response to the optimal perturbations [see (20)], which are both proportional to the inverse of κ in the simple model (Fig. 10, right). These results are generally consistent with the GCM computations, in which the optimal delay and the ocean response also decrease when horizontal diffusion increases. However, this decrease in the ocean GCM is not as fast as in the idealized model, probably because the former incorporates many more relevant dynamical factors other than diffusion.

5. Conclusions

In this study we have explored the growth of initial disturbances in an ocean GCM from the point of view of decadal climate variability and predictability. We address several key questions: Is it possible to modify the initial conditions (slightly) to reduce model bias at a given time interval in the future? More generally, how strongly and how fast can initial disturbances in the ocean grow on decadal time scales? These two questions

are complementary since they both depend on the characteristics of the transient increase of initial disturbances in the ocean.

We show that indeed adding small temperature or salinity anomalies to the model initial conditions at depth in the Southern Ocean can reduce the model bias (discrepancy between the ocean observations and the model output) 1–2 decades after model initialization. The suitable initial perturbations are found via an optimization technique. We use several approaches, including a linear approximation and a more accurate nonlinear iterative approach assuming weak amplitudes of the initial disturbances. These methods generate similar results for anomalies below 0.2 K and allow for a reduction in the model bias by 10%–15% as evaluated by an integral measure for the entire ocean (which computes an average ''distance'' between the model output and the observed climatology).

Although the overall bias reduction is relatively modest, in some regions of the upper ocean the reduction is much larger, exceeding several kelvins and persisting for over a decade. The impacts are especially noticeable in the Southern Ocean and in the North Atlantic. Moreover, the 10%–15% limit is reached simply because the linear and iterative approaches become inapplicable for initial perturbations greater than 0.2 K, and fully nonlinear techniques are required. We anticipate that the method of conditional nonlinear optimal perturbations (e.g., Mu et al. 2004; Mu and Zhang 2006; Mu et al. 2007) will allow a much more substantial reduction of the bias.

Even though the initial motivation of this study was to reduce model bias over a given time interval, our results on the increase of initial disturbances have much broader implications for decadal climate predictability. Specifically, our findings imply that initial errors in the deep ocean smaller than 0.1 K can lead to errors of several kelvins in the upper ocean after about 14 yr. In a linear framework, an error of about 0.7 K in the initial conditions could nearly double the total discrepancy between the model output and oceanic data over the same time. Such an enhanced sensitivity to the initial conditions in the ocean GCM gives rise to an uncertainty in the ocean state after 1–2 decades, setting a decadal predictability barrier.

Potentially, our simple expression for the most efficient transient change time scale, $\tau_{\text{opt}} = L^2/(\kappa\pi^2)$ [see (18)], could be used to estimate the predictability barrier due to large-scale ocean dynamics in other models as well. This time scale corresponds to the typical damping of the largest-scale temperature anomalies in the Southern Ocean by horizontal diffusion (L being the meridional wavelength of the anomalies). In high-resolution models, the horizontal diffusivity κ should be replaced by an effective coefficient of diffusion due to resolved eddies.

The strong transient increase of the initial disturbances comes from the system's nonnormality related to the existence of a strong mean meridional temperature gradient in the upper ocean (such a gradient is absent in the deep ocean). This creates a clear asymmetry in the dynamics; initial perturbations in the deep ocean are especially effective in generating anomalies in the upper ocean on decadal time scales. These anomalies include a large-scale quasi-stationary wave pattern (of stationary eddies) originating in the Southern Ocean. As demonstrated by our idealized model, the strength of this mean thermal gradient sets the magnitude of the transient changes of the observation–model discrepancy and thus controls the impact of initial errors. These conclusions are consistent with the higher sensitivity to perturbations of the Southern Ocean and the North Atlantic evident in GCM calculations (these two regions have the strongest mean meridional temperature gradient in the upper ocean).

When considering the roles of both temperature and salinity, one finds another nonnormal factor contributing to the transient change mechanisms. The optimal initial perturbations show constructive effects of temperature and salinity on density; however, perturbations at the peak of their intensity correspond to density anomalies dominated by temperature but partially compensated by salinity. The former effect is explained by the fact that a stronger density anomaly, with constructive contributions of temperature and salinity, can induce a stronger geostrophic flow and thus stimulate the transient change more efficiently. The latter effect is due to the partial compensation (with respect to density) between the mean meridional gradients of temperature and salinity that typically occurs in the upper ocean. Such nonnormal behavior is consistent with the analyses of Sévellec and Fedorov (2013a) and Sévellec and Fedorov (2013b, manuscript submitted to *Prog. Oceanogr.*).

As previously discussed, applying linear or weakly nonlinear frameworks constitutes one of the limitations of this study. Nevertheless, all of our main conclusions hold as long as we consider the transient increase of small initial disturbances (below 0.2 K). The second limitation is the use of an ocean-only model, rather than a fully coupled GCM. However, strong similarities between calculations with the mixed and flux boundary conditions increase confidence in the robustness of our results.

The strong sensitivity of the upper ocean to small temperature or salinity disturbances in the deep ocean apparent on decadal time scales highlights the necessity for collecting more measurements from larger depths of the ocean. Even though Argo floats have contributed to the vast expansion of oceanic data coverage down to 2000 m, our results indicate that the greatest sensitivity

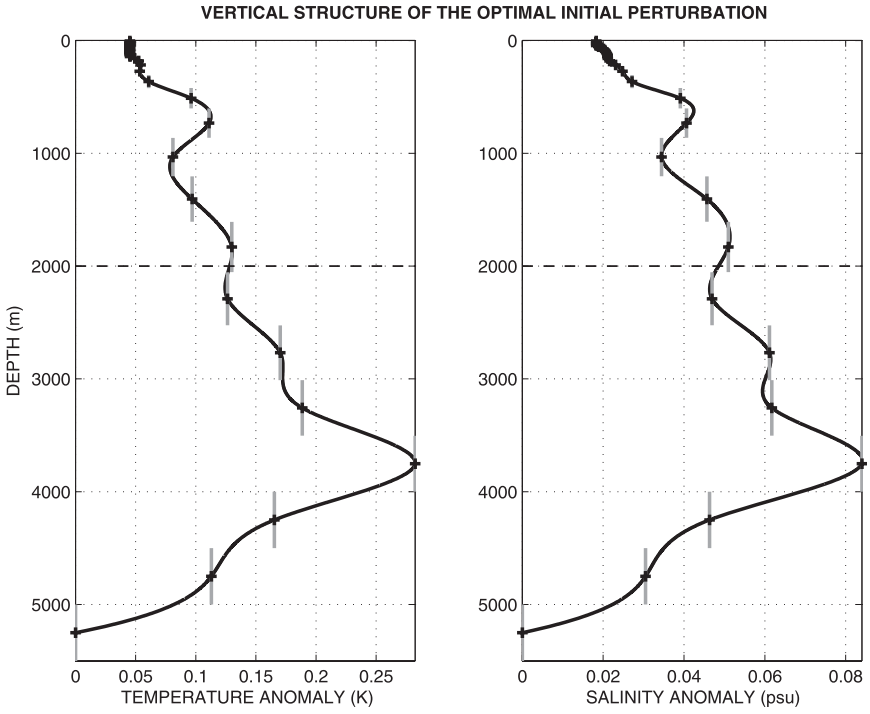

FIG. 11. The vertical structure and magnitude of the optimal initial perturbation in Fig. 5 as a function of depth for (left) temperature and (right) salinity. The results are presented as the model data at each level of the ocean GCM (small crosses) connected by a cubic spline interpolation (black solid line). Gray vertical intervals indicate the thickness of the model levels; the horizontal dot–dashed line indicates the typical depth limit of Argo floats (2000 m). In effect, this plot shows the sensitivity of the upper-ocean temperature to disturbances at different depths. The strongest sensitivity develops for disturbances located at a depth of about 3700 m.

occurs for disturbances at depths between 3000 and 4000 m. This is evident from Fig. 11, which summarizes the main results of our study and, in effect, shows the sensitivity of the upper ocean to disturbances at different depths. This figure implies that, in order to facilitate decadal climate prediction, we will need major investments in in situ measurements in the deep ocean, lest decadal prediction will be out of reach.

Acknowledgments. This research was supported by grants from NSF (OCE-0901921), DOE Office of Science (DE-SC0007037), the David and Lucile Packard Foundation, and the Ti Ammo project funded through the French CNRS/INSU/LEFE program. We thank two anonymous reviewers and the editor, Anand Gnanadesikan, for their comments and suggestions.

APPENDIX

An Expansion Procedure for Optimal Perturbations

In this appendix we consider a perturbation $|\mathbf{u}\rangle$ of the trajectory $|\overline{\mathbf{U}}\rangle$ and expand it as

$$|\mathbf{u}\rangle = \sum_i \epsilon^i |\mathbf{u}_i\rangle = \epsilon|\mathbf{u}_1\rangle + \epsilon^2|\mathbf{u}_2\rangle + \cdots,$$

where ϵ is a small nondimensional parameter (proportional to the amplitude of the initial perturbation), $|\mathbf{u}_i\rangle$ are of the same order of magnitude, and $|\mathbf{u}\rangle$ is a function of time and space.

Then, the bias of the perturbed state can be written as

$$\begin{aligned}\|\text{bias}_{\text{pert}}\| &= \langle \mathbf{U}_D - (\overline{\mathbf{U}} + \mathbf{u})|\mathbf{S}|\mathbf{U}_D - (\overline{\mathbf{U}} + \mathbf{u})\rangle,\\ &= \langle \mathbf{U}_D - \overline{\mathbf{U}}|\mathbf{S}|\mathbf{U}_D - \overline{\mathbf{U}}\rangle - 2\epsilon\langle \mathbf{U}_D - \overline{\mathbf{U}}|\mathbf{S}|\mathbf{u}_1\rangle\\ &\quad + \epsilon^2(\langle \mathbf{u}_1|\mathbf{S}|\mathbf{u}_1\rangle - 2\langle \mathbf{U}_D - \overline{\mathbf{U}}|\mathbf{S}|\mathbf{u}_2\rangle)\\ &\quad + 2\epsilon^3\langle \mathbf{u}_1|\mathbf{S}|\mathbf{u}_2\rangle + \epsilon^4\langle \mathbf{u}_2|\mathbf{S}|\mathbf{u}_2\rangle + O(\epsilon^3).\end{aligned} \tag{A1}$$

The first-order problem for reducing the bias has been already solved in section 3 (i.e., we found initial conditions for $|\mathbf{u}_1\rangle$ that would reduce the term proportional to ϵ in (A1) at a later time).

Next, we need to solve the second-order problem: we need to find initial conditions for $|\mathbf{u}_2\rangle$ that would reduce the term proportional to ϵ^2 in Eq. (A1). Using an expression similar to (9) we obtain

$$\langle \mathbf{U}_D - \overline{\mathbf{U}} | \mathbf{S} | \mathbf{u}_2(\tau_{\text{opt}}) \rangle = \frac{\langle \mathbf{u}_1(\tau_{\text{opt}}) | \mathbf{S} | \mathbf{u}_1(\tau_{\text{opt}}) \rangle}{2},$$

$$\langle \mathbf{U}_D - \overline{\mathbf{U}} | \mathbf{S}\mathbf{M}(-\tau_{\text{opt}}) | \mathbf{u}_2(0) \rangle = \frac{1}{2} \frac{\langle \mathbf{U}_D - \overline{\mathbf{U}} | \mathbf{S}\mathbf{M}(-\tau_{\text{opt}}) \mathbf{S}^{-1} \mathbf{M}^{\dagger}(\tau_{\text{opt}}) \mathbf{S}\mathbf{M}(-\tau_{\text{opt}}) \mathbf{S}^{-1} \mathbf{M}^{\dagger}(\tau_{\text{opt}}) \mathbf{S} | \mathbf{U}_D - \overline{\mathbf{U}} \rangle}{\langle \mathbf{U}_D - \overline{\mathbf{U}} | \mathbf{S}\mathbf{M}(-\tau_{\text{opt}}) \mathbf{S}^{-1} \mathbf{M}^{\dagger}(\tau_{\text{opt}}) \mathbf{S} | \mathbf{U}_D - \overline{\mathbf{U}} \rangle},$$

$$|\mathbf{u}_2(0)\rangle = \frac{1}{2} \frac{\mathbf{S}^{-1} \mathbf{M}^{\dagger}(\tau_{\text{opt}}) \mathbf{S} | \mathbf{u}_1(\tau) \rangle}{[\langle \mathbf{U}_D - \overline{\mathbf{U}} | \mathbf{S}\mathbf{M}(-\tau_{\text{opt}}) \mathbf{S}^{-1} \mathbf{M}^{\dagger}(\tau_{\text{opt}}) \mathbf{S} | \mathbf{U}_D - \overline{\mathbf{U}} \rangle]^{1/2}}.$$

This procedure can be repeated iteratively to compute higher-order corrections to the initial perturbations as long as ϵ is sufficiently small. In the main body of the paper, in Fig. 8 (gray line), we used (A1) while neglecting terms of the third and higher order in ϵ.

REFERENCES

Arzel, O., T. Huck, and A. Colin de Verdière, 2006: The different nature of the interdecadal variability of the thermohaline circulation under mixed and flux boundary conditions. *J. Phys. Oceanogr.,* **36,** 1703–1718.

Blanke, B., and P. Delecluse, 1993: Variability of the tropical Atlantic Ocean simulated by a general circulation model with two different mixed-layer physics. *J. Phys. Oceanogr.,* **23,** 1363–1388.

Carton, J. A., G. Chepurin, X. Cao, and B. Giese, 2000: A simple ocean data assimilation analysis of the global upper ocean 1950–95. Part I: Methodology. *J. Phys. Oceanogr.,* **30,** 294–309.

Colin de Verdière, A., 1988: Buoyancy driven planetary flow. *J. Mar. Res.,* **46,** 215–265.

Collins, M., and B. Sinha, 2003: Predictability of decadal variations in the thermohaline circulation and climate. *Geophys. Res. Lett.,* **30,** 1306, doi:10.1029/2002GL016504.

Czeschel, L., D. P. Marshall, H. L. Johnson, 2010: Oscillatory sensitivity of Atlantic overturning to high-latitude forcing. *Geophys. Res. Lett.,* **37,** L10601, doi:10.1029/2010GL043177.

Farrell, B. F., and A. M. Moore, 1992: An adjoint method for obtaining the most rapidly growing perturbation to oceanic flows. *J. Phys. Oceanogr.,* **22,** 338–349.

——, and P. J. Ioannou, 1996a: Generalized stability theory. Part I: Autonomous operators. *J. Atmos. Sci.,* **35,** 2025–2040.

——, and ——, 1996b: Generalized stability theory. Part II: Nonautonomous operators. *J. Atmos. Sci.,* **53,** 2041–2053.

Ganachaud, A., and C. Wunsch, 2000: Improved estimates of global ocean circulation, heat transport and mixing from hydrographic data. *Nature,* **408,** 453–457.

Gent, P. R., and J. C. McWilliams, 1990: Isopycnal mixing in ocean circulation model. *J. Phys. Oceanogr.,* **20,** 150–155.

Gnanadesikan, A., and R. Hallberg, 2000: On the relationship of the circumpolar current to Southern Hemisphere winds in coarse-resolution ocean models. *J. Phys. Oceanogr.,* **30,** 2013–2034.

Griffies, S. M., and K. Bryan, 1997: A predictability study of simulated North Atlantic multidecadal variability. *Climate Dyn.,* **13,** 459–487.

Grötzner, A., M. Latif, A. Timmermann, and R. Voss, 1999: Interannual to decadal predictability in a coupled ocean–atmosphere circulation model. *J. Climate,* **12,** 2607–2624.

Hallberg, R., and A. Gnanadesikan, 2001: An exploration of the role of transient eddies in determining the transport of a zonally reentrant current. *J. Phys. Oceanogr.,* **31,** 3312–3330.

Hasselmann, K., 1976: Stochastic climate models. Part I. Theory. *Tellus,* **28,** 473–485.

Hawkins, E., and R. Sutton, 2009a: Decadal predictability of the Atlantic Ocean in a coupled GCM: Forecast skill and optimal perturbations using linear inverse modeling. *J. Climate,* **22,** 3960–3978.

——, and ——, 2009b: The potential to narrow uncertainty in regional climate predictions. *Bull. Amer. Meteor. Soc.,* **90,** 1095–1107.

Heimbach, P., C. Wunsch, R. M. Ponte, G. Forget, C. Hill, and J. Utke, 2011: Timescales and regions of the sensitivity of Atlantic meridional volume and heat transport: Toward observing system design. *Deep-Sea Res. II,* **58,** 1858–1879.

Held, I. M., 1983: Stationary and quasi-stationary eddies in the extratropical troposphere: Theory. *Large-Scale Dynamical Processes in the Atmosphere,* B. J. Hoskins, and R. P. Pearce, Eds., Academic Press, 127–168.

Huck, T., and G. K. Vallis, 2001: Linear stability analysis of three-dimensional thermally-driven ocean circulation: Application to interdecadal oscillations. *Tellus,* **53A,** 526–545.

Keenlyside, N. S., M. Latif, J. Jungclaus, L. Kornblueh, and E. Roeckner, 2008: Advancing decadal-scale climate prediction in the North Atlantic sector. *Nature,* **453,** 84–88.

Killworth, P. D., D. B. Chelton, and R. A. de Szoeke, 1997: The speed of observed and theoretical long extratropical planetary waves. *J. Phys. Oceanogr.,* **27,** 1946–1966.

Latif, M., and T. P. Barnett, 1996: Decadal climate variability over the North Pacific and North America: Dynamics and predictability. *J. Climate,* **9,** 2407–2423.

——, M. Collins, H. Pohlmann, and N. Keenlyside, 2006: A review of predictability studies of Atlantic sector climate on decadal time scales. *J. Climate,* **19,** 5971–5986.

Levitus, S., 1989: Interpentadal variability of temperature and salinity at intermediate depths of the North Atlantic Ocean, 1970-1974 versus 1955-1959. *J. Geophys. Res.,* **94,** 9679–9685.

Lorenz, E. N., 1963: Deterministic non-periodic flow. *J. Atmos. Sci.,* **20,** 130–141.

——, 1965: Predictability study of 28-variable atmospheric model. *Tellus,* **17,** 321–333.

Madec, G., and M. Imbard, 1996: A global ocean mesh to overcome the North Pole singularity. *Climate Dyn.,* **12,** 381–388.

——, P. Delecluse, M. Imbard, and C. Lévy, 1998: OPA 8.1 ocean general circulation model reference manual. Institut Pierre-Simon Laplace Tech. Rep. 11, 91 pp.

Marotzke, J., P. Welander, and J. Willebrand, 1988: Instability and multiple steady states in a meridional-plane model of the thermohaline circulation. *Tellus,* **40A,** 162–172.

Marti, O., and Coauthors, 2010: Key features of the IPSL ocean atmosphere model and its sensitivity to atmospheric resolution. *Climate Dyn.,* **34,** 1–26.

Meehl, G. A., and Coauthors, 2009: Decadal prediction: Can it be skillful? *Bull. Amer. Meteor. Soc.,* **90,** 1467–1485.

Moore, A. M., J. Vialard, A. T. Weaver, D. L. T. Anderson, R. Kleeman, and J. R. Johnson, 2003: The role of air–sea interaction in controlling the optimal perturbations of low-frequency tropical coupled ocean–atmosphere modes. *J. Climate,* **16,** 951–968.

Mu, M., and Z. Zhang, 2006: Conditional nonlinear optimal perturbations of a two-dimensional quasigeostrophic model. *J. Atmos. Sci.,* **63,** 1587–1604.

——, L. Sun, and H. A. Dijkstra, 2004: The sensitivity and stability of the ocean's thermohaline circulation to finite-amplitude perturbations. *J. Phys. Oceanogr.,* **34,** 2305–2315.

——, W. Duan, and B. Wang, 2007: Season-dependent dynamics of nonlinear optimal error growth and El Niño-Southern Oscillation predictability in a theoretical model. *J. Geophys. Res.,* **112,** D10113, doi:10.1029/2005JD006981.

Olbers, D., D. Borowski, C. Völker, and J.-O. Wölff, 2004: The dynamical balance, transport and circulation of the Antarctic Circumpolar Current. *Antarct. Sci.,* **16,** 439–470.

Palmer, T. N., 1999: A nonlinear dynamical perspective on climate prediction. *J. Climate,* **12,** 575–591.

Pohlmann, H., M. Botzet, M. Latif, A. Roesch, M. Wild, and P. Tschuck, 2004: Estimating the decadal predictability of a coupled AOGCM. *J. Climate,* **17,** 4463–4472.

Qin, X., and M. Mu, 2011: Influence of conditional nonlinear optimal perturbations sensitivity on typhoon track forecasts. *Quart. J. Roy. Meteor. Soc.,* **138,** 185–197, doi:10.1002/qj.902.

Redi, M. H., 1982: Oceanic isopycnal mixing by coordinate rotation. *J. Phys. Oceanogr.,* **12,** 1154–1158.

Rivière, G., B. L. Hua, and P. Klein, 2001: Influence of the beta-effect on non-modal baroclinic instability. *Quart. J. Roy. Meteor. Soc.,* **127,** 1375–1388.

Rossby, C. G., 1939: Relation between variations in the intensity of the zonal circulation of the atmosphere and the displacements of the semi-permanent centers of action. *J. Mar. Res.,* **2,** 38–55.

Sévellec, F., and A. V. Fedorov, 2010: Excitation of SST anomalies in the eastern equatorial Pacific by oceanic optimal perturbations. *J. Mar. Res.,* **68,** 1–28.

——, and ——, 2013a: The leading, interdecadal eigenmode of the Atlantic meridional overturning circulation in a realistic ocean model. *J. Climate,* **26,** 2160–2183.

——, M. Ben Jelloul, and T. Huck, 2007: Optimal surface salinity perturbations influencing the thermohaline circulation. *J. Phys. Oceanogr.,* **37,** 2789–2808.

——, T. Huck, M. Ben Jelloul, N. Grima, J. Vialard, and A. Weaver, 2008: Optimal surface salinity perturbations of the meridional overturning and heat transport in a global ocean general circulation model. *J. Phys. Oceanogr.,* **38,** 2739–2754.

——, ——, ——, and J. Vialard, 2009: Nonnormal multidecadal response of the thermohaline circulation induced by optimal surface salinity perturbations. *J. Phys. Oceanogr.,* **39,** 852–872.

Smith, D. M., S. Cusack, A. W. Colman, C. K. Folland, G. R. Harris, and J. M. Murphy, 2007: Improved surface temperature prediction for the coming decade from a global climate model. *Science,* **317,** 796–799.

Solomon, S., D. Qin, M. Manning, M. Marquis, K. Averyt, M. M. B. Tignor, H. L. Miller Jr., and Z. Chen, Eds., 2007: *Climate Change 2007: The Physical Science Basis.* Cambridge University Press, 996 pp.

Stone, P. H., 2004: Climate prediction: The limits of ocean models. *The State of the Planet: Frontiers and Challenges in Geophysics, Geophys. Monogr.,* Vol. 150, Amer. Geophys. Union, 259–267.

Strogatz, S. H., 1994: *Nonlinear Dynamics and Chaos with Applications to Physics, Biology, Chemistry and Engineering.* Perseus, 498 pp.

Talley, L. D., J. L. Reid, and P. E. Robbins, 2003: Data-based meridional overturning streamfunctions for the global ocean. *J. Climate,* **16,** 3213–3226.

Taylor, K. E., R. J. Stouffer, and G. A. Meehl, 2012: An overview of CMIP5 and the experiment design. *Bull. Amer. Meteor. Soc.,* **93,** 485–498.

Tziperman, E., and P. J. Ioannou, 2002: Transient growth and optimal excitation of thermohaline variability. *J. Phys. Oceanogr.,* **32,** 3427–3435.

——, L. Zanna, and C. Penland, 2008: Nonnormal thermohaline circulation dynamics in a coupled ocean–atmosphere GCM. *J. Phys. Oceanogr.,* **38,** 588–604.

Weaver, A. T., J. Vialard, and D. L. T. Anderson, 2003: Three- and four-dimensional variational assimilation with a general circulation model of the tropical Pacific Ocean. Part I: Formulation, internal diagnostics, and consistency checks. *Mon. Wea. Rev.,* **131,** 1360–1378.

Wunsch, C., 2010: Observational network design for climate. *Proc. OceanObs'09,* Venice, Italy, ESA, WPP-306. [Available online at http://www.oceanobs09.net/proceedings/pp/4C2-Wunsch-OceanObs09.pp.41.pdf.]

Zanna, L., and E. Tziperman, 2005: Nonnormal amplification of the thermohaline circulation. *J. Phys. Oceanogr.,* **35,** 1593–1605.

——, and ——, 2008: Optimal surface excitation of the thermohaline circulation. *J. Phys. Oceanogr.,* **38,** 1820–1830.

——, P. Heimbach, A. M. Moore, and E. Tziperman, 2010: The role of ocean dynamics in the optimal growth of tropical SST anomalies. *J. Phys. Oceanogr.,* **40,** 983–1003.

——, ——, ——, and ——, 2011: Optimal excitation of interannual Atlantic meridional overturning circulation variability. *J. Climate,* **24,** 413–427.

Zhou, F., and M. Mu, 2011: The impact of verification area design on tropical cyclone targeted observations based on the CNOP method. *Adv. Atmos. Sci.,* **28,** 997–1010.